Geochemistry, Geophysics, Geosystems®

RESEARCH ARTICLE
10.1029/2023GC011010

# Controls on Mineral Formation in High pH Fluids From the Lost City Hydrothermal Field

**Karmina A. Aquino[1,2], Gretchen L. Früh-Green[1], Stefano M. Bernasconi[1], Tomaso R. R. Bontognali[3,4], Anneleen Foubert[5], and Susan Q. Lang[6]**

[1]Department of Earth Sciences, ETH Zürich, Zürich, Switzerland, [2]Now at Department of Science and Technology—Philippine Nuclear Research Institute, Quezon City, Philippines, [3]Space Exploration Institute, Neuchâtel, Switzerland, [4]Department of Environmental Sciences, University of Basel, Basel, Switzerland, [5]Department of Geosciences—Geology, University of Fribourg, Fribourg, Switzerland, [6]Woods Hole Oceanographic Institution, Woods Hole, MA, USA

**Abstract** Although the serpentinite-hosted Lost City hydrothermal field (LCHF) was discovered more than 20 years ago, it remains unclear whether and how the presence of microbes affects the mineralogy and textures of the hydrothermal chimney structures. Most chimneys have flow textures comprised of mineral walls bounding paleo-channels, which are preserved in inactive vent structures to a varying degree. Brucite lines the internal part of these channels, while aragonite dominates the exterior. Calcite is also present locally, mostly associated with brucite. Based on a combination of microscopic and geochemical analyses, we interpret brucite, calcite, and aragonite as primary minerals that precipitate abiotically from mixing seawater and hydrothermal fluids. We also observed local brucite precipitation on microbial filaments and, in some cases, microbial filaments may affect the growth direction of brucite crystals. Brucite is more fluorescent than carbonate minerals, possibly indicating the presence of organic compounds. Our results point to brucite as an important substrate for microbial life in alkaline hydrothermal systems.

**Plain Language Summary** Water-serpentinite reactions at the Lost City hydrothermal field (LCHF) are considered similar to the interactions between seawater and volcanic rocks of the early Earth. The vent fluids that form as a result of this interaction are rich in organic compounds that serve as food and hydrogen that provides energy for microbial life. Systems such as Lost City are ideal sites for investigating processes relevant to early life on Earth. Dense microbial communities live in the mineral structures that form from mixing between vent fluids and seawater at the LCHF. The effect of these microbial inhabitants on the mineralogy and textures of the hydrothermal chimneys is still unknown. This study aims to better understand the mineralogy of the hydrothermal chimneys at Lost City and the relationships between microbes and minerals. Calcite and brucite form in the interior of the chimneys, while aragonite forms on the exterior. Brucite forms inorganic mineral membranes that bound cavities where microbes may live. Unlike calcite and aragonite, brucite is spatially closely associated with microbial activity.

**Key Points:**

- Lost City hydrothermal chimneys preserve flow textures defined by mineral membranes bounding paleo-channels and form a network of cavities
- The backbone of the chimney structure is initially brucite. Carbonates precipitate on brucite as the chimneys continue to form
- Brucite is the preferred substrate for the growth of microbial biofilms within the chimneys

**Supporting Information:**

Supporting Information may be found in the online version of this article.

**Correspondence to:**

K. A. Aquino,
kaaquino@pnri.dost.gov.ph

**Citation:**

Aquino, K. A., Früh-Green, G. L., Bernasconi, S. M., Bontognali, T. R. R., Foubert, A., & Lang, S. Q. (2024). Controls on mineral formation in high pH fluids from the Lost City hydrothermal field. *Geochemistry, Geophysics, Geosystems*, *25*, e2023GC011010. https://doi.org/10.1029/2023GC011010

Received 20 APR 2023
Accepted 18 JAN 2024



## 1. Introduction

As seawater enters the oceanic crust at depths of up to 13 km (Tao et al., 2020), it is heated and reacts chemically with the surrounding rocks, altering the composition of both the seawater and the rocks along the fluid flow path (Alt, 1995; German & Von Damm, 2003). This thermally driven circulation of seawater via faults and fractures in the oceanic crust that occurs at or near the over ~60,000 km long mid-ocean ridge system has important consequences in plate tectonics, the matter and energy transfer between the lithosphere and the hydrosphere, the geochemistry of the ocean, the composition of the oceanic crust, and the early origin of life (Früh-Green et al., 2022; Humphris et al., 1995). The Lost City hydrothermal field (LCHF) exemplifies a type of hydrothermal system associated with the serpentinization of ultramafic rocks and venting at low to moderate temperatures (<100°C). The LCHF is regarded as a possible analogue alkaline hydrothermal vent (AHV) of the Archean ocean because of stark parallels in terms of temperature, pH, chemistry, and host rocks. The LCHF is located on the southern wall of the Atlantis Massif at 30°N, ~15 km west of the Mid-Atlantic Ridge (MAR) (Figure 1). The southern section of the Atlantis massif is composed of serpentinized peridotites interspersed with minor gabbroic bodies (Blackmann et al., 2002). Hydrothermal activity at Lost City has been active for likely more than 30,000 years and possibly >100,000 years (Früh-Green et al., 2003; Ludwig et al., 2011; Ternieten et al., 2021b). Fluid flow is controlled by seawater infiltration and discharge via steeply dipping normal faults and deformation

10.1029/2023GC011010

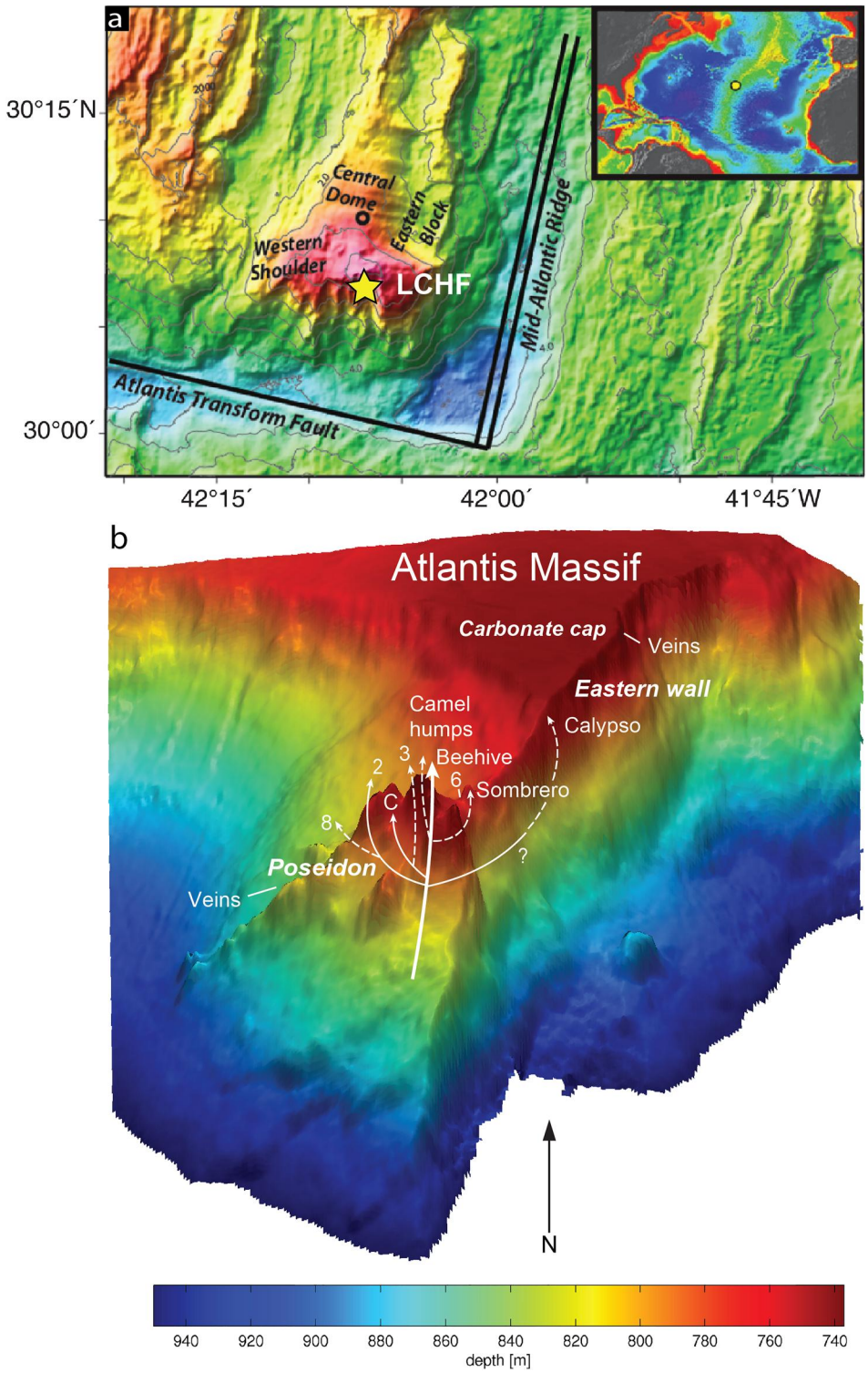


**Figure 1.** Map of the study site. (a) The Lost City hydrothermal field is located on the southern wall of the Atlantis Massif at the inside corner of the intersection between the Mid-Atlantic Ridge and the Atlantis Transform Fault. Inset shows the location of the LCHF at 30°N. (b) 3D image showing the location of the different vent sites and fluid flow paths indicating the relationship between the vents based on sulfur geochemistry (Aquino et al., 2022). Most of the vents at the center of the field comprise the Poseidon structure. Several other vents are located along the eastern wall. Note: thick solid line—first order vent; thin solid line—second order vents; thin dashed lines —third order vents. See text for more details.

fabrics in the serpentinite basement within the 100-m thick detachment shear zone responsible for the exhalation of the massif (Karson et al., 2006; Kelley et al., 2005). The serpentinization-influenced vent fluids at Lost City are warm (up to ~116°C), alkaline, and rich in hydrogen, methane, and formate, and show a systematic compositional variability from the central to the more peripheral parts of the field (Allen & Seyfried, 2004; Aquino et al., 2022; Foustoukos et al., 2008; Kelley et al., 2005; Lang et al., 2010, 2012; Proskurowski et al., 2006, 2008; Seyfried et al., 2015).

Carbonate-brucite hydrothermal towers with spire- or flange-like morphologies form up to 60 m-high structures when vent fluids and seawater mix (Früh-Green et al., 2003; Kelley et al., 2001; Ludwig et al., 2006). Young, active chimneys consist predominantly of brucite, calcite and aragonite, characterized by low $^{87}Sr/^{86}Sr$ and trace element contents (Aquino et al., 2024; Früh-Green et al., 2003; Kelley et al., 2001; Ludwig et al., 2006). Mineralogical and geochemical changes have been shown to accompany the chimneys during aging (Ludwig et al., 2006). However, it is unclear whether spatial compositional variability in the vent fluids may have an additional influence on the compositions of the resulting carbonate-brucite structures. In our companion paper, we show that the degree of vent fluid-seawater mixing affects chimney mineralogy such that calcite and brucite precipitate from a vent-fluid rich solution. Aragonite, on the other hand, forms when the fluid has a higher proportion of seawater (Aquino et al., 2024). Progressive reaction with seawater during aging of the chimneys when vent fluid flow wanes results in the conversion of aragonite to calcite, dissolution of brucite, and an increase in $^{87}Sr/^{86}Sr$ and trace element contents (Ludwig et al., 2006).

The organic compounds and hydrogen in the Lost City vent fluids provide carbon sources and reducing power to a dense community of microbes in the chimneys and subseafloor (Brazelton et al., 2006, 2022; Konn et al., 2009; Lang & Brazelton, 2020; Lang et al., 2018; Mcgonigle et al., 2020). The interior of the chimneys and relatively higher temperature structures are dominated by the methane-cycling Lost City *Methanosarcinales*, while the exterior and lower temperature chimneys are inhabited by a more diverse group of sulfur- and methane-oxidizers, including the filamentous *Eubacteria* and the methanotrophic *Archaea* (ANME-1) (Brazelton et al., 2006; Schrenk et al., 2004). The microbial inhabitants of the vent fluids include the hyperthermophilic *Thermococcales* and *Crenarcheota*, and the sulfate-reducing bacteria *Thermodesulfovibrionales* (Brazelton et al., 2006, 2022). These microbes represent the subsurface ecosystem at Lost City and share key metabolic strategies with microbes from other serpentinite-hosted systems (Brazelton et al., 2022), suggesting that biogeochemical processes occurring in those alkaline systems are analogous. For example, the first microbial colonizers of hydrothermal chimneys at the Prony Bay Hydrothermal Field, a shallow coastal serpentinite-hosted system in New Caledonia, have been shown to play an important role in the early formation of the chimney structures (Pisapia et al., 2017). It is conceivable that a similar process is occurring at Lost City. At present, the role of thick microbial biofilms that populate the chimneys (Lang & Brazelton, 2020) during the construction of the chimneys at Lost City is unclear.

In this study, we document the mineralogy and fabric of hydrothermal chimneys collected from actively venting structures at LCHF, highlighting spatial variabilities within a chimney as well as among chimneys across the field. In addition, we aim to determine whether microbial communities at Lost City play a role in chimney development and to investigate the presence and extent of biologically influenced mineralization. We highlight the importance of brucite during chimney development and show that brucite comprises inorganic mineral membranes that represent flow structures in young, active chimneys. Our results suggest that there may be an important link between brucite mineralization and the incorporation of organic matter in the hydrothermal structures.

## 2. Sampling Sites

Hydrothermal vent structures at Lost City have various morphologies, such as pinnacles and spires, as well as parasitic cone- and flange-structures (Früh-Green et al., 2003; Kelley et al., 2001, 2005; Ludwig et al., 2006). Spires range in size from a few meters up to tens of meters in height, with the most prominent structure *Poseidon*, which is a composite of multiple actively venting structures, rising up to 60 m above the seafloor (Figure 1). Vent structures that comprise Poseidon include Marker 3, Camel Humps, Beehive, Marker 2, Marker C, and Marker 8 (Figures 1 and 2a–2f; Table S1 in Supporting Information S1). Ludwig et al. (2006) focused on active and inactive samples from the Poseidon structure in order to investigate the mineralogical and geochemical transformation during aging of the chimneys. In this work, we sampled a relatively large number of samples mostly from actively venting structures, including the relatively lower temperature vents away from Poseidon, in order to determine

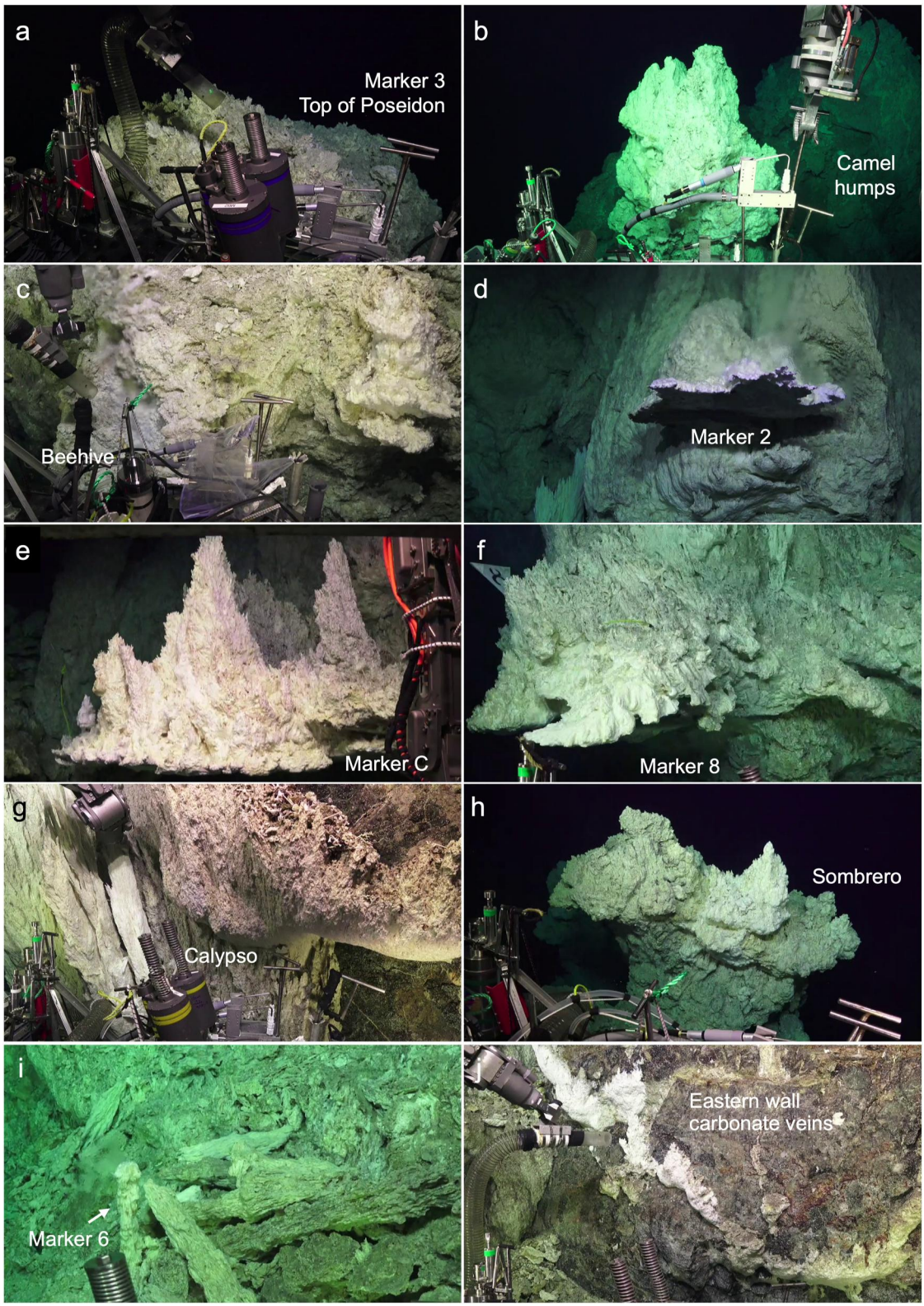


**Figure 2.** Photos of the Lost City vent sites investigated. (a) Marker 3 and (b) Camel Humps are sites located near the top of the Poseidon structure. (c) The Beehive structure vents the hottest fluids at the LCHF, but was no longer present during sampling in 2018. (d) Marker 2, Marker C, and (f) Marker 8 are flange vents on the Poseidon structure. Vents along the eastern wall include (g) Calypso, (h) Sombrero, and (i) Marker 6. (j) Carbonate vein along the eastern wall. Vent locations are given in Figure 1. Images courtesy of S. Lang, UofSC/NSF/remotely operated vehicle Jason/2018 © WHOI.

any spatial mineralogical variability within a chimney structure independent of aging. Marker 3 and Camel Humps are two adjacent sites (~several meters apart) near the top of the Poseidon structure, yet the vent fluids have distinct geochemistry and microbial compositions (Aquino et al., 2022; Brazelton et al., 2022). Beehive is a parasitic structure with a morphology resembling a beehive, and was sampled in previous field campaigns (Früh-Green et al., 2003; Kelley et al., 2001, 2005; Proskurowski et al., 2006). It vents the hottest fluids (up to 96–116° C) that are most representative of the first-order, unaltered endmember fluid at Lost City (Aquino et al., 2022; Kelley et al., 2005). The Beehive structure was missing during sampling in 2018; thus, we collected chimney samples directly at the site where vigorous fluid flow occurs, presumably representing the interior of the previous Beehive structure (Figure 2c). Markers 2, C, and 8 are parasitic flange-like structures growing horizontally from Poseidon and trapping warm vent fluids within the downward facing flanges (Figures 2d–2f). Actively venting chimney structures that we sampled along the steep northeast trending escarpment, referred to as the eastern wall, include the vent structures Calypso, Marker 6, and Sombrero (Figures 1 and 2g–2i). Calypso is a fresh spire that grows directly from the serpentinite wall, while Marker 6 is a small, delicate spire on top of inactive chimney debris. We sampled fresh chimney growth atop a bigger, older structure at the Sombrero site. Although Marker 6 and Sombrero are located away from Poseidon, sulfur geochemistry of the fluids suggests that these structures share a common fluid flow path with Beehive (Aquino et al., 2022). In contrast, Calypso has vent fluid compositions with a stronger seawater influence (Aquino et al., 2022). A few structures along the eastern wall that did not show evidence of venting at the time of sampling were also sampled. We also sampled carbonate veins or fissure filling deposits west of Marker 8 as well as along the eastern wall (Figures 1 and 2j).

Aquino et al. (2022) grouped the vents into four groups based on their sulfur geochemistry, $H_2$ concentrations, and location within the field. The low sulfide groups, which include Beehive, Camel humps, Marker 6, and Sombrero, are located close to the center of the field and have the lowest sulfide and the highest $H_2$ and sulfate contents (Figure 1). Sulfide concentrations generally increase with distance from the center of the field in the moderate sulfide (Markers C and 3), high sulfide (Markers 2 and 8), and eastern wall groups (Calypso and veins). At the same time, $H_2$ and sulfate concentrations increase toward the more peripheral vent groups. This systematic compositional variability is attributed to the progressive sulfate reduction along the different flow paths (Aquino et al., 2022; Kelley et al., 2005; Lang et al., 2012; Proskurowski et al., 2006). Aquino et al. (2022) also suggested that all of the Lost City vent fluids are derived from a primary (first-order) vent fluid with a composition similar to that sampled at Beehive. This first-order vent fluid is then modified to form second- and third-order vents via continued sulfate reduction and incorporation of seawater sulfate (Figure 1).

## 3. Methods

### 3.1. Sampling

Sampling was carried out in September 2018 during the Return to the Lost City expedition (*R/V Atlantis* cruise AT42-01) with the remotely operated vehicle (ROV) *Jason*. We sampled sites that had been previously investigated over the course of 20 years of studying Lost City, including Beehive and sites named after field markers (e.g., Marker C) placed in 2003 (Kelley et al., 2005), most of which are associated with the Poseidon structure (Figure 1). The structures Sombrero and Calypso, located near the eastern wall, were sampled for the first time in 2018. We collected a total of 37 samples (31 chimneys and 6 carbonate veins) mostly from structures where active venting and non-ambient water temperatures were observed, as well as a few non-venting structures and fissure-filling deposits (Figure 1; see Section 2). Upon recovery, the samples were described macroscopically in terms of texture, color, and the presence of flow structures or layering. Each sample was given a unique ID, which included the *Jason* dive number, date and time of collection, and sample type (e.g., J.1109.19Sep.0756 CHIM for a chimney sample collected on 19 September 2018, 07:56 GMT during *Jason* Dive 1109). For simplicity, we use a shortened version of the sample ID giving the dive number and time of collection (e.g., 1109–0756). The samples were divided onboard amongst the science party members and each of these subsamples was assigned a cruise ID (e.g., sample 1109–0756 is further subdivided into samples with cruise ID LC01349, LC01353, etc.). In some cases, samples show heterogeneities in color, texture, and/or mineralogy. Distinct layers or parts of the samples were sampled and analyzed separately (e.g., LC01349a, LC01349b) for mineralogy and geochemistry. Carbonate minerals were also separated by hand picking under a binocular microscope and were analyzed separately for their stable isotope compositions. The geochemistry of the samples and mineral separates are presented in Aquino et al. (2024).

### 3.2. Analytical Methods

Mineralogy was determined using an X-ray diffractometer with a CuKα radiation and a LynxEye detector (Bruker AXS D8 Advance Powder XRD, Bruker Corporation, Billerica, USA) at the Institute of Geochemistry and Petrology, ETH Zürich. We used a scan range of 5–90° $2\theta$ with a step size of 0.02 and scan time of 0.8 s per step. Identification of the minerals was performed using the ICDD Sieve+ (International Center for Diffraction Data, USA) automatic peak search software, which is integrated into the ICDD PDF-2 database. Quantification of the mineral phases was carried out by a full-profile Rietveld refinement method (Rietveld, 1969) using the program Siroquant version 3.0 (Seitronics, Australia), while the calculation of the full-width at half maximum of representative brucite diffraction data was performed using OriginPro (https://www.originlab.com/origin).

Thin sections were prepared from resin-impregnated samples for conventional transmitted microscopy using a polarizing microscope (Carl Zeiss Microscopy GmbH, Göttingen, Germany) at ETH Zürich. Fluorescence microscopy was carried out on the same thin sections on a Nikon Eclipse Ci Pol microscope (Nikon Instruments, Inc.) at the Department of Geosciences, University of Fribourg. The samples were excited using blue UV light (472 nm wavelength) combined with a green fluorescence emission filter (520 nm wavelength).

For scanning electron microscopy (SEM), two sets of samples were prepared. The first set was fixed onboard upon collection in 4% paraformaldehyde in 1X phosphate buffered saline solution or 1X glycerol tris-EDTA in 15- or 50-ml falcon tubes. Onshore, these were cut into 2-3 mm-sized pieces, placed inside Eppendorf tubes, shock frozen in a liquid nitrogen bath, and freeze-dried for at least 2 hr at ETH Zürich. The second set of samples was not fixed prior to mounting onto the sample holders. Prior to SEM analyses, all samples were coated with Pt-Pd. Microimaging and semi-quantitative elemental analyses were carried out on a FEI Quanta 200F Field Emission Gun - Scanning Electron Microscope (Field Electron and Ion, Co., ThermoFischer Scientific) and an Energy Dispersive X-ray spectrometer (EDAX Octane Super) system at the Scientific Center for Optical and Electron Microscopy (ScopeM, ETH Zürich). Analyses were performed using secondary electron and back-scattered electron detectors at accelerating voltages ranging from 7 to 15 KV.

Micro-X-ray computed tomography (μX-CT) analyses of samples were performed using the Bruker-SkyScan 2211 μX-ray CT at the Department of Geosciences, University of Fribourg. Image acquisition was performed using an X-ray source operating at 33–90 kV, 310–600 μA, and with a step size of 0.2°. Individual shadow images with a pixel resolution of 10–20 μm and 1.2–6.5 μm were obtained using a flatpanel and a CCD (charge-coupled device) detector, respectively. During scanning, a 0.5 mm Al-filter was used to reduce beam hardening effects. Shadow images were reconstructed using the Bruker-SkyScan NRecon software (version 1.6.9.18).

Radiocarbon ages of the samples were determined using an elemental analyzer coupled to a Miniscale Carbon Dating system (MICADAS) accelerator mass spectrometer (AMS) equipped with a gas-ion source (Synal et al., 2007) at the Laboratory of Ion Beam Physics, ETH Zürich following the methodology detailed in Ruff et al. (2010) and Wacker et al. (2010). Carbonate samples were transferred to vacutainers, flushed with He for 10 min, and reacted with 85% $H_3PO_4$ and injected directly into the gas source of the AMS. Standard normalization and blank correction were made with the Nist SRM 4990C standard (Oxalic Acid II) and IAEA C-1 (radiocarbon blank $CO_2$), respectively. The precision of the analysis estimated from repeated measurements of IAEA-C2 and coral CSTD during each run is better than ±5% on a modern standard. Radiocarbon data are reported as a fraction of modern carbon ($F^{14}C$) and $^{14}C$ ages (Reimer et al., 2004).

## 4. Results

### 4.1. Mineralogy and Textures

Descriptions of the samples can be found in Table S2 in Supporting Information S1 and the mineralogy is plotted in Figures 3 and 4 and Figure S1 in Supporting Information S1. Hand specimen photos are in Figure 5; overview micro-CT images and SEM images are shown in Figures 6 and 7 and in Figure S2 in Supporting Information S1. The active chimneys are composed of varying proportions of aragonite, calcite, and brucite, similar to assemblages that have previously been described (Früh-Green et al., 2003; Kelley et al., 2001; Ludwig et al., 2006). The relative proportions of these minerals vary substantially. Bulk samples (Figures 3 and 4) are dominated by brucite and aragonite, with 21 out of 42 having more than 50% brucite and 16 having more than 50% aragonite. Calcite is

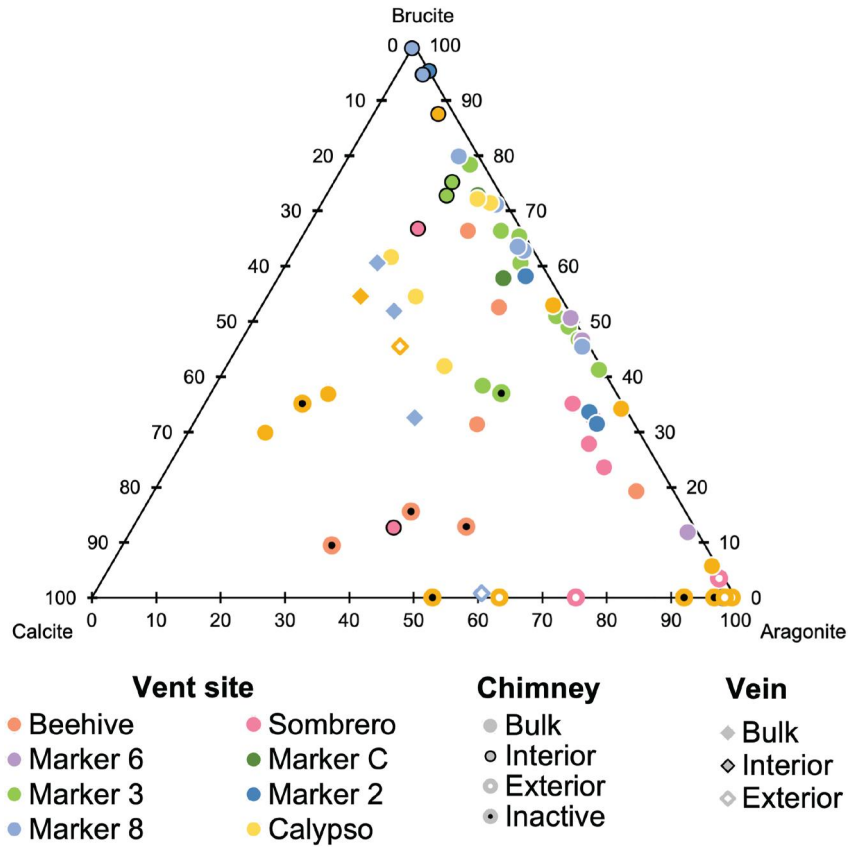


**Figure 3.** Ternary diagram showing the mineralogy of LCHF chimneys and veins. The samples are composed of variable amounts of brucite, calcite, and aragonite. Subsamples collected from the interior (dark outline) are often brucite-rich, whereas subsamples from the exterior (white infill) are aragonite-rich. Samples from the previously defined low sulfide vent group (Aquino et al., 2022) include Beehive and Sombrero and are relatively calcite-rich compared to the samples collected from the moderate sulfide group (Marker C and Marker 3) and from the high sulfide group (Marker 2 and Marker 8). Chimneys from low temperature vents along the eastern wall include Calypso and the carbonate veins and are also calcite-rich. A version of this figure sorted by vent group is found in Figure S1 in Supporting Information S1.

a minor component in the actively venting chimneys and only 3 bulk samples were observed to contain more than 30% calcite. Two of these are from chimney structures along the eastern wall, and one is from Beehive (Figure 3).

Most of the LCHF chimney samples are heterogenous and friable at the hand specimen scale, showing intricate intermixing between distinctly bright white, fine-grained brucite and cream- to dark cream-colored carbonates that have anastomosing fibrous morphologies often reflecting relict flow structures (Table S2 in Supporting Information S1). Flow textures are preserved either by the direction of crystal growth and/or as mineral channel walls assuming to bound former fluid flow conduits (Figures 5–7; Figure S3 in Supporting Information S1). A few samples exhibit a feathery or quill-like texture produced by acicular aragonite crystals sharing a common nucleation point (Table S2 in Supporting Information S1; Figure 6a; Figure S3 in Supporting Information S1) with the direction of crystal growth parallel to the direction of fluid flow. This texture may be concealed by abundant fine-grained brucite, giving the sample an overall chalk-like appearance (Figures 5b and 5c).

The majority of the samples appear fibrous in the hand specimen and preserve mineral membrane-bound relict flow paths or fluid conduits (Figures 6b, 6c, and 7a; Figure S4 in Supporting Information S1). The thinnest mineral membranes and the interior of these channel walls are made up of several tens of microns thick brucite upon which later-formed minerals precipitate (Figures 6 and 7a; Figures S3–S5 in Supporting Information S1). The brucite channel walls are made up of individual brucite plates less than 1 μm thick forming a reticulated lattice-like texture (Figures S5e and S5f in Supporting Information S1). Aragonite precipitating on the channel walls often forms botryoidal aggregates or fans comprised of acicular crystals that coalesce into crusts/layers

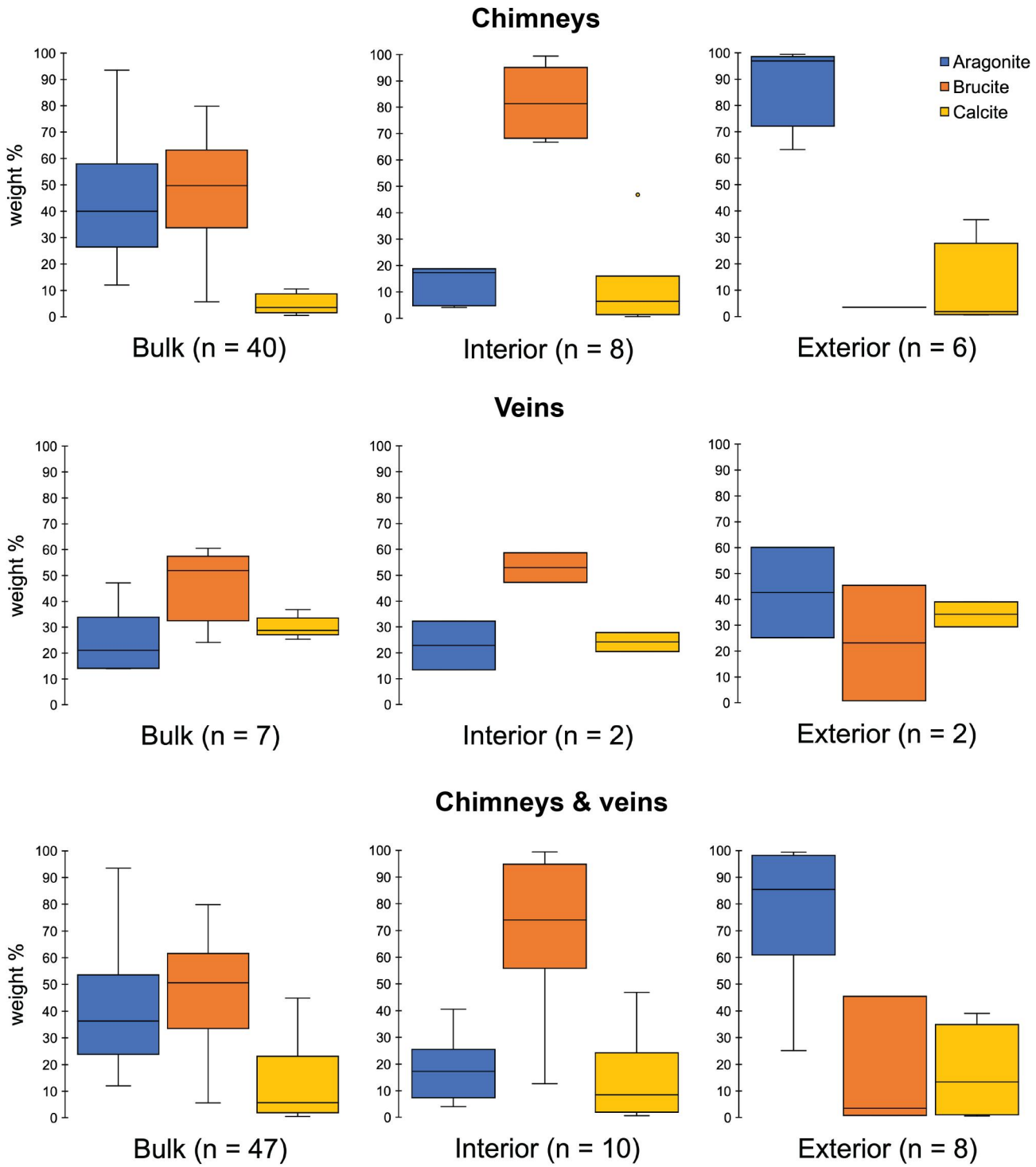


**Figure 4.** Box plot of the mineralogy of the bulk, interior and exterior parts of the chimneys and veins investigated. The range is bounded by the minimum and maximum abundance for each mineral, while the bottom and top of the box are the first and third quartiles, respectively. The middle line represents the mean mineral abundance.

(Figures S4a–S4e in Supporting Information S1), while calcite and brucite occur as globular to botryoidal aggregate textures (Figure 8).

Like the chimneys, the veins are composed of brucite, aragonite, and calcite (Figure 4), whereby brucite is the dominant mineral in almost all the bulk vein samples. In general, the veins have more calcite (25%–34%) and less

10.1029/2023GC011010

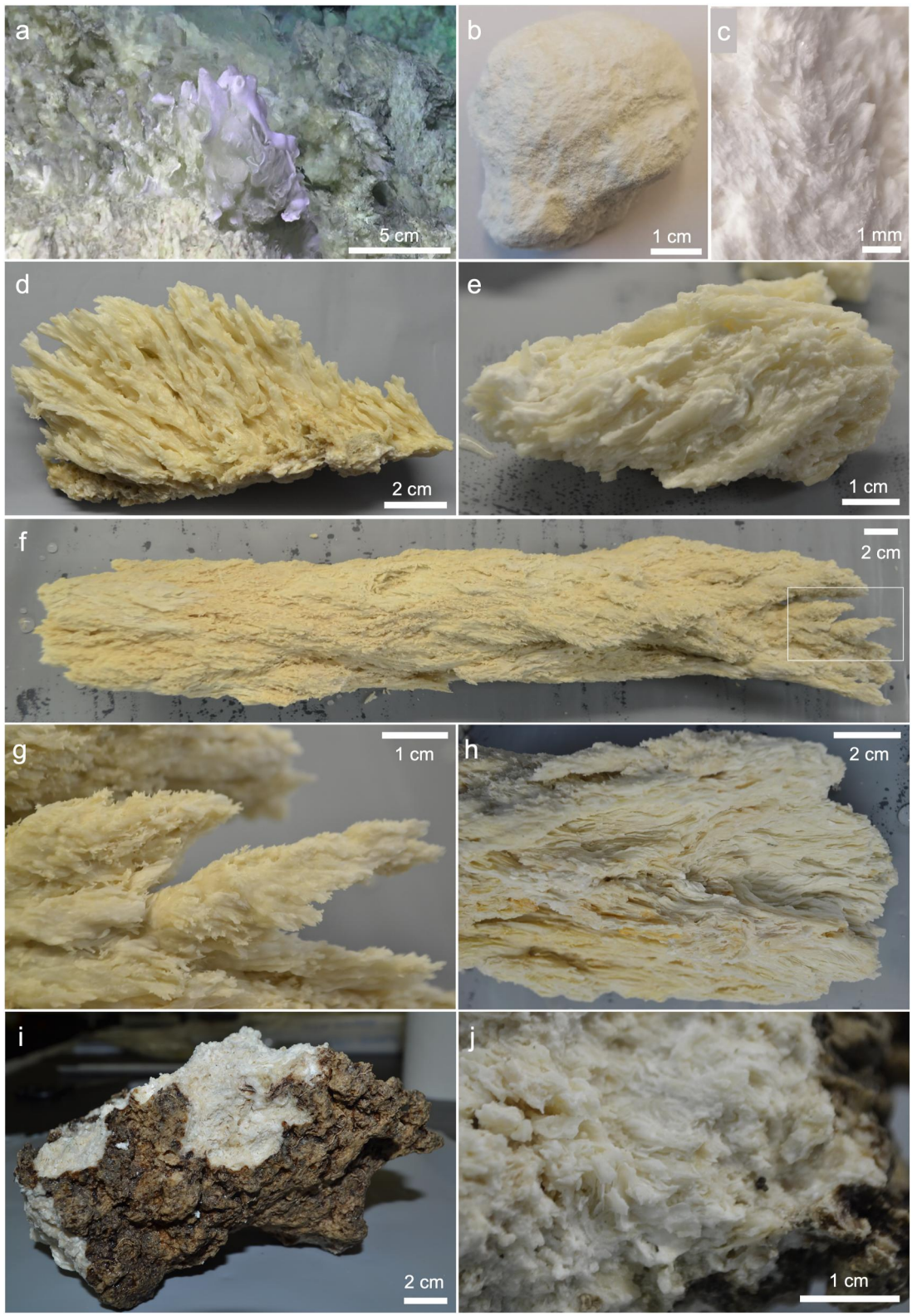


**Figure 5.**

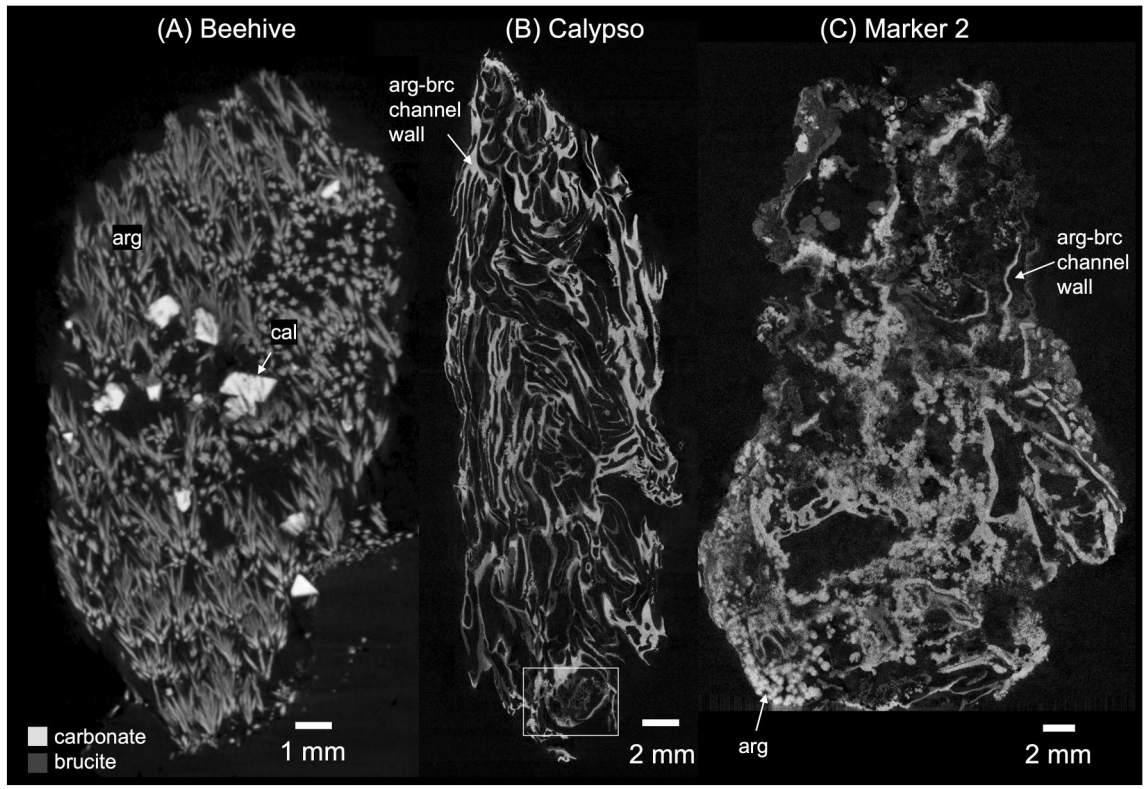


**Figure 6.** Overview micro-CT images of flow structures. (a) Flow textures in 1109–1057 from Beehive are preserved by acicular aragonite. Rhombohedral calcite (brighter phase) is also present throughout the sample. (b) Fresh spire from Calypso (1108–2002) is composed of interconnected mineral membranes which are made up of brucite and aragonite and bound paleo-fluid flow conduits. (c) In 1107–2314, these mineral channel walls form microcompartments where mineral precipitation is observed. Note that brucite has a lower density than calcium carbonate and appears darker in the micro-CT scan. The detail of the white box can be found in Figure S13 in Supporting Information S1.

aragonite (15%–47%) compared to the chimneys. In contrast to the delicate and highly porous chimneys, the carbonate veins are more lithified and their surfaces are dark gray to dark brown (Figure 5i). However, the interior of the veins still preserves the cream color and fibrous, sinuous textures similar to those of the chimneys (Figure 5j).

### 4.2. Spatial Variability

The chimneys exhibit textural and mineralogical differences between the interior and exterior parts of the spires. Almost all the subsamples from the interior of the chimney structures (7 out of 8) are composed of 70%–99% of brucite (Figure 4). In the hand specimen, the brucite-rich spire or flange interior is bright white and have a powdery appearance (Figures S6 and S7 in Supporting Information S1). Under the SEM, brucite commonly exhibits botryoidal aggregate textures of individual platy or prismatic crystals that are often associated with calcite (up to 47%) and sometimes with a Mg-silicate phase (Figures 8c and 8d; Figures S6 and S8 in Supporting Information S1). In contrast to the interior, the exterior of the chimneys ($n = 6$) is primarily aragonite-rich (Figure 4). Structures that are considered to be recently inactive that appear young but where no venting was observed during sampling ($n = 4$) have more calcite and less brucite than active chimneys (Figure 3). Carbonate

**Figure 5.** Examples of flow texture preservation at LCHF. (a) Sinuous white mineral surfaces formed by active fluid flow at Marker 3. (b) Hand specimen of sample 1109–1057 from Beehive. As the Beehive structure was no longer present during sampling, this sample was collected from the interior of what used to be the Beehive-like structure, where vigorous active venting was observed. The sample is covered by fine-grained brucite giving it a chalk-like appearance. (c) In places where brucite is dislodged or partially dissolved, the sample has a feathery flow texture formed by the direction of aragonite growth. (d) Sample 1107–1714 from Marker 3 showing a fresh spire with sinuous flow structures that have grown on a fine-grained brucite-rich layer. (e) Small piece of a large spire (1107–2314) collected next to the venting flange at Marker 2. (f) Fresh, delicate spire (1108–2002) from Calypso. (g) Detail of white box shown in (f). (h) Bottom of the sample showing sinuous flow texture. (i) Vein or fissure-filling deposit (1110–0838) west of Marker 8. (j) Inside the dark brown weathered crust is a cream-colored interior with a fibrous flow texture.

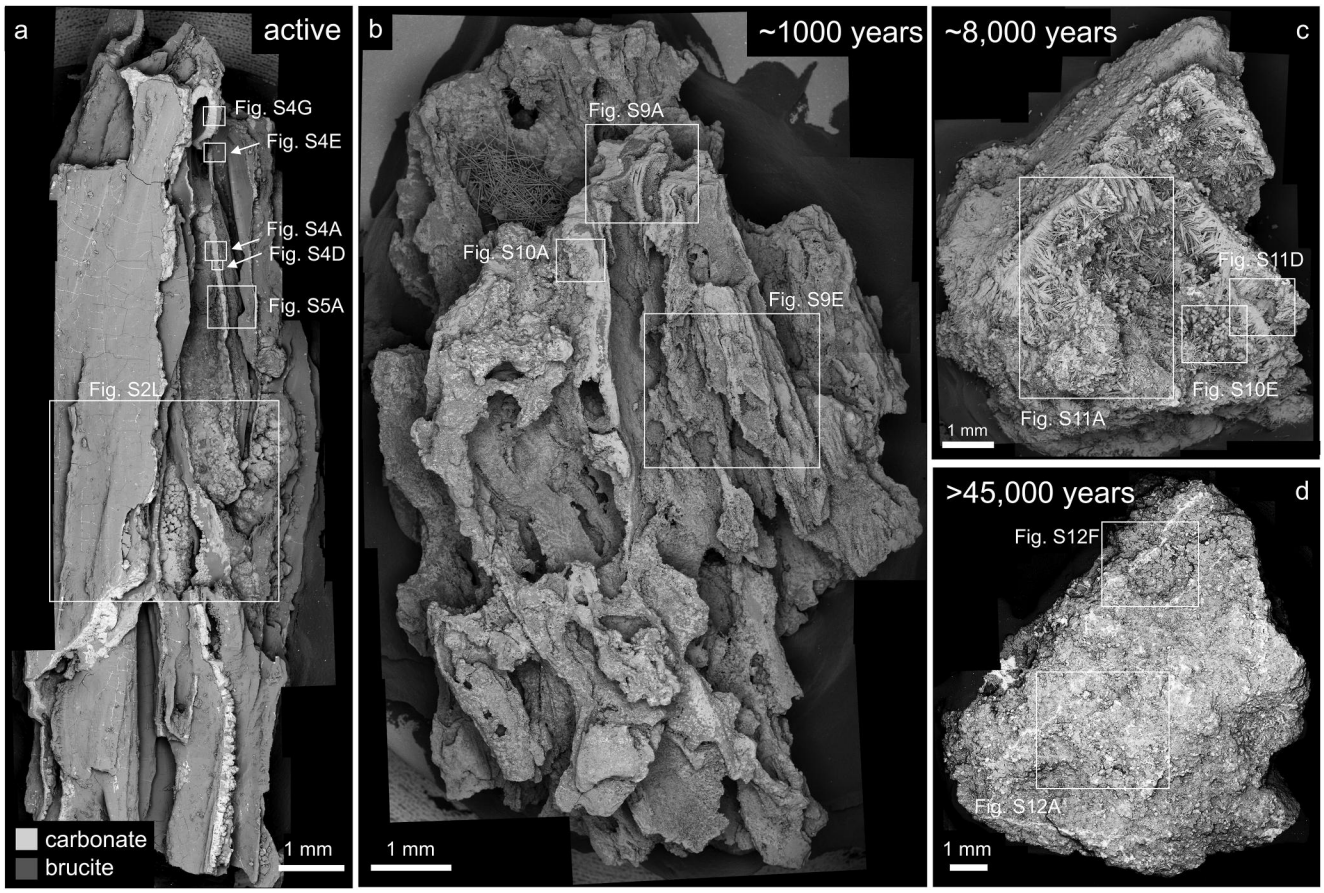


**Figure 7.** SEM photo mosaic showing the preservation of flow textures in active, inactive, and extinct samples. (a) Active spire from Calypso (1108–2002) is made up of aragonite-brucite channel walls. Aragonite and brucite-calcite aggregates have precipitated on these mineral channel walls. (b) In a recently extinct sample (3651–1231), channel flow structures are preserved. Brucite is still present locally and the sample is made up mostly of aragonite. (c) 3871–1512 is a ~8,000-year-old sample. Here, channel walls are not clear but can still be recognized by subparallel aragonite crystals. Brucite is absent in this sample. (d) In 3872–1544, an extinct sample, massive and relict flow textures are absent. Brucite is absent and most of the aragonite has been recrystallized to calcite. Approximate ages based on $^{14}C$ and/or $^{230}Th$ obtained from Früh-Green et al. (2003) and Ludwig et al. (2011), and this study are also shown. Note: See Figures S4, S5, S10–S12 in Supporting Information S1 for more details on these samples.

veins are also slightly more brucite-rich in the interior while the exterior has slightly more aragonite, although the difference is less pronounced compared to the chimneys (Figure 4). In addition to the spatial differences observed between the interior and exterior of the chimneys, there is a marked difference between the central and the more peripheral sites of the hydrothermal field near the eastern wall (Figure 3). Except for one sample from Beehive and one from Marker 3, samples from the sites at or near Poseidon (Figure 1) have calcite contents that are often less than 10%, whereas many samples from the eastern wall and Calypso (Figure 3) are composed of more than 20% calcite.

### 4.3. Radiocarbon Ages

The radiocarbon ages of selected active and inactive structures from Lost City are listed in Table 1. Except for two samples, most of the samples from actively venting structures have $^{14}C$ ages that are less than ~500 years and several samples yielded modern radiocarbon contents ($F^{14}C > 1.0$), demonstrating that the carbon incorporated into the chimneys is derived from seawater. The $^{14}C$ ages of minerals collected from the same sample vary by as much as 3,000 years although there is no systematic difference between aragonite and calcite from the same chimney structure. In general, samples from the low sulfide vent group defined by Aquino et al. (2022) (see Section 2) have slightly lower $F^{14}C$ values than samples from the moderate and high sulfide groups. The two carbonate veins yielded variable radiocarbon ages. The carbonate vein sampled near the eastern wall has a modern age, whereas the vein located west of Marker 8 has a $^{14}C$ age of >2,000 years. The two inactive chimney

10.1029/2023GC011010

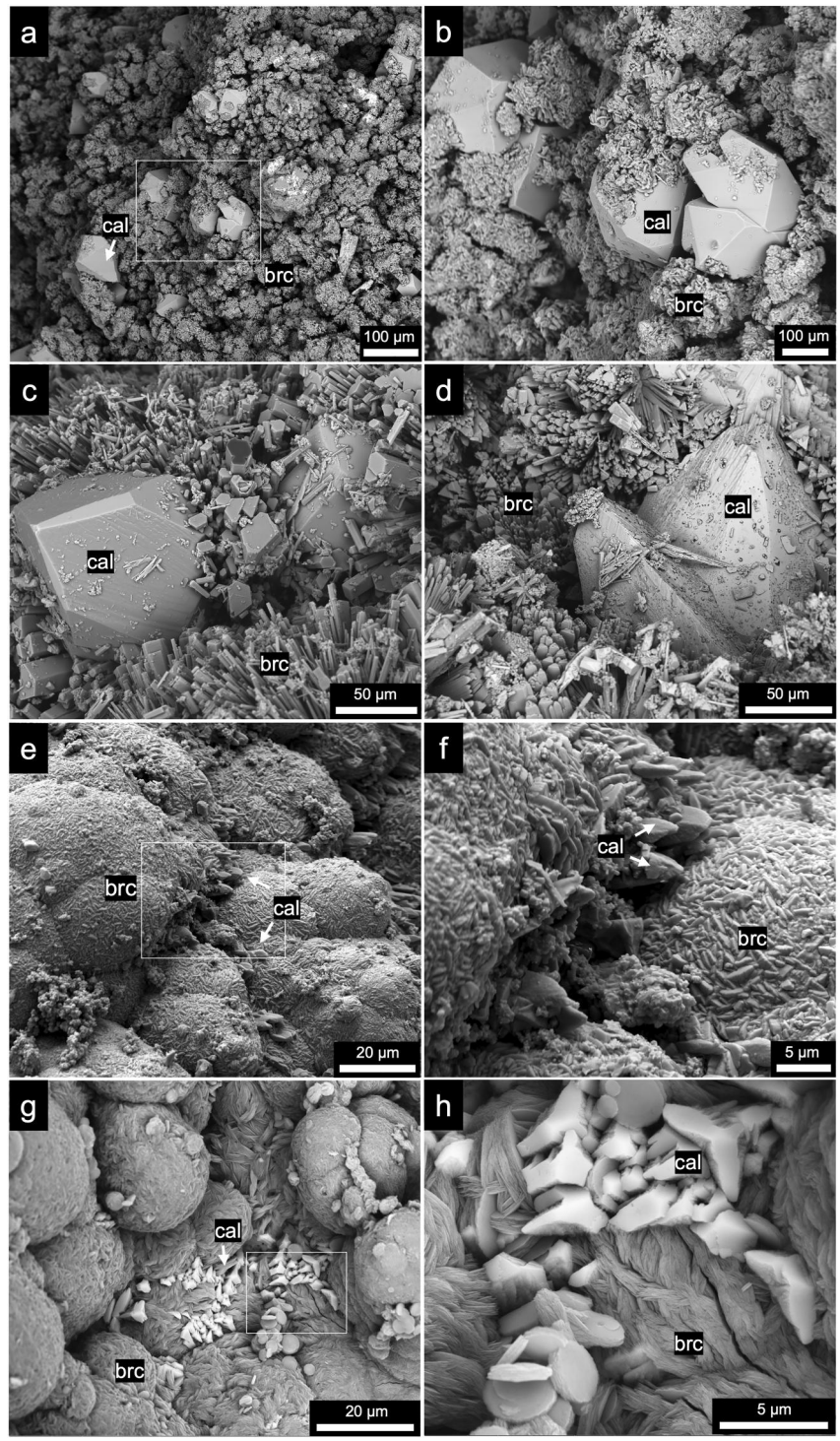


**Figure 8.** SEM images highlighting the association of calcite and brucite in young, active chimneys. (a) Calcite (cal) and fine-grained brucite (brc) in sample 1109–1057 from Beehive. (b) Detail of white box in (a). (c, d) In 1109–0743 (Sombrero), brucite occurs as prisms or needles with (c) hexagonal or (d) triangular cross-sections. In both cases, calcite is observed together with brucite. See Figures S6d and S6e in Supporting Information S1 for the general location of these images. (e) Botryoidal aggregate of brucite plates and subhedral calcite in 1110–0611 (Marker 8). See Figure S7e in Supporting Information S1 for the general location of this image. (f) Detail of white box in (e). (g) Botryoidal brucite and unusually shaped calcite in 1108–2002 (Calypso). See Figure S5b in Supporting Information S1 for the general location of this image. (h) Detail of the white box in (g).

**Table 1**
*Radiocarbon Ages of Chimney and Vein Minerals From Lost City*

| Cruise ID | Site | Mineralogy | $F^{14}C$ | $^{14}C$ age | $^{230}Th$ age[a] |
|---|---|---|---|---|---|
| Low sulfide group | | | | | |
| LC01291 | Beehive | Aragonite | 0.684 ± 0.01 | 3,053 ± 71 | |
| LC01291 | Beehive | Calcite | 0.957 ± 0.01 | 353 ± 63 | |
| LC02489 | Sombrero | Aragonite | 0.988 ± 0.01 | 94 ± 62 | |
| LC02489 | Sombrero | Calcite | 0.975 ± 0.01 | 204 ± 64 | |
| LC02555 | Marker 6 | Aragonite | 0.944 ± 0.01 | 459 ± 67 | |
| Moderate sulfide group | | | | | |
| LC01796 | Marker C | Aragonite | 1.030 ± 0.01 | −239 ± 64 | |
| LC01796 | Marker C | Calcite | 1.019 ± 0.01 | −149 ± 63 | |
| LC00226 | Marker 3 | Aragonite | 1.006 ± 0.01 | −44 ± 64 | |
| LC00226 | Marker 3 | Calcite | 0.878 ± 0.01 | 1,042 ± 66 | |
| High sulfide group | | | | | |
| LC00311 | Marker 2 | Aragonite | 1.018 ± 0.01 | −141 ± 64 | |
| LC02604 | Calypso | Bulk chimney | 1.014 ± 0.01 | −111 ± 63 | |
| Eastern wall group | | | | | |
| LC01336a | Carbonate vein | Bulk vein | 1.009 ± 0.01 | −75 ± 63 | |
| LC01849a | West of Marker 8 | Bulk vein | 0.765 ± 0.01 | 2,153 ± 69 | |
| Inactive structures | | | | | |
| 3651-1231 | Poseidon | Calcite/Aragonite | | 585 ± 35[b] | 1,286 ± 1,278 |
| 3871-1512 | Southwest of field | Calcite/Aragonite | 0.356 ± 0.00 | 8,290 ± 92 | 15,989 ± 3,766 |
| 3872-1544 | Southwest of field | Calcite | 0.003 ± 0.00 | 45,471 ± 2,418 | 169,516 ± 14,167 |

[a]From Ludwig et al. (2011). [b]From Früh-Green et al. (2003).

structures have radiocarbon ages of 8,290 ± 92 and 45,471 ± 2,418 years, which are less than the $^{230}Th$ ages of the same samples (15,989 and 169,516 years, respectively; Ludwig et al., 2011).

### 4.4. Inactive Chimney Textures

Inactive vent structures preserve textures similar to active hydrothermal chimneys to a varying degree (Figures 7b and 7c). In a more recently inactive chimney (sample 3651–1231, 585–1,286 years old, Früh-Green et al., 2003; Ludwig et al., 2011), mineral channel wall structures are still clearly preserved (Figure 7b; Figure S9 in Supporting Information S1). Like in active chimneys, brucite lines the channel walls although evidence of partial brucite dissolution can be observed (Figure S9d in Supporting Information S1), and aragonite needles occur perpendicular to brucite (Figures S9a–S9d in Supporting Information S1). Older inactive chimneys (>10,000 years, Ludwig et al., 2011) are characterized by the absence of brucite and the transformation of fine needles of aragonite to larger calcite crystals (Figure S10 in Supporting Information S1). In sample 3871–1512, despite the absence of brucite, relict channel walls are still present as linear features formed by subparallel aragonite needles (Figure 7c; Figure S11 in Supporting Information S1; $^{230}Th$ age = 15,989, Ludwig et al., 2011). In contrast, in an extinct sample (3872–1544, $^{230}Th$ age ~170,000 years, Ludwig et al., 2011), the primary mineral textures and channel walls are no longer recognizable (Figure 7d; Figure S12 in Supporting Information S1). In general, with age, the channels of inactive chimneys are progressively filled with increasing number of broken off carbonate crystals and microfossils.

### 4.5. Microbial Biofilms

The hydrothermal chimneys contain microbial biofilms comprised of cells and extracellular polymeric substances (EPS) of various morphologies and fabrics that range from simple filaments to complex networks of fibers, and

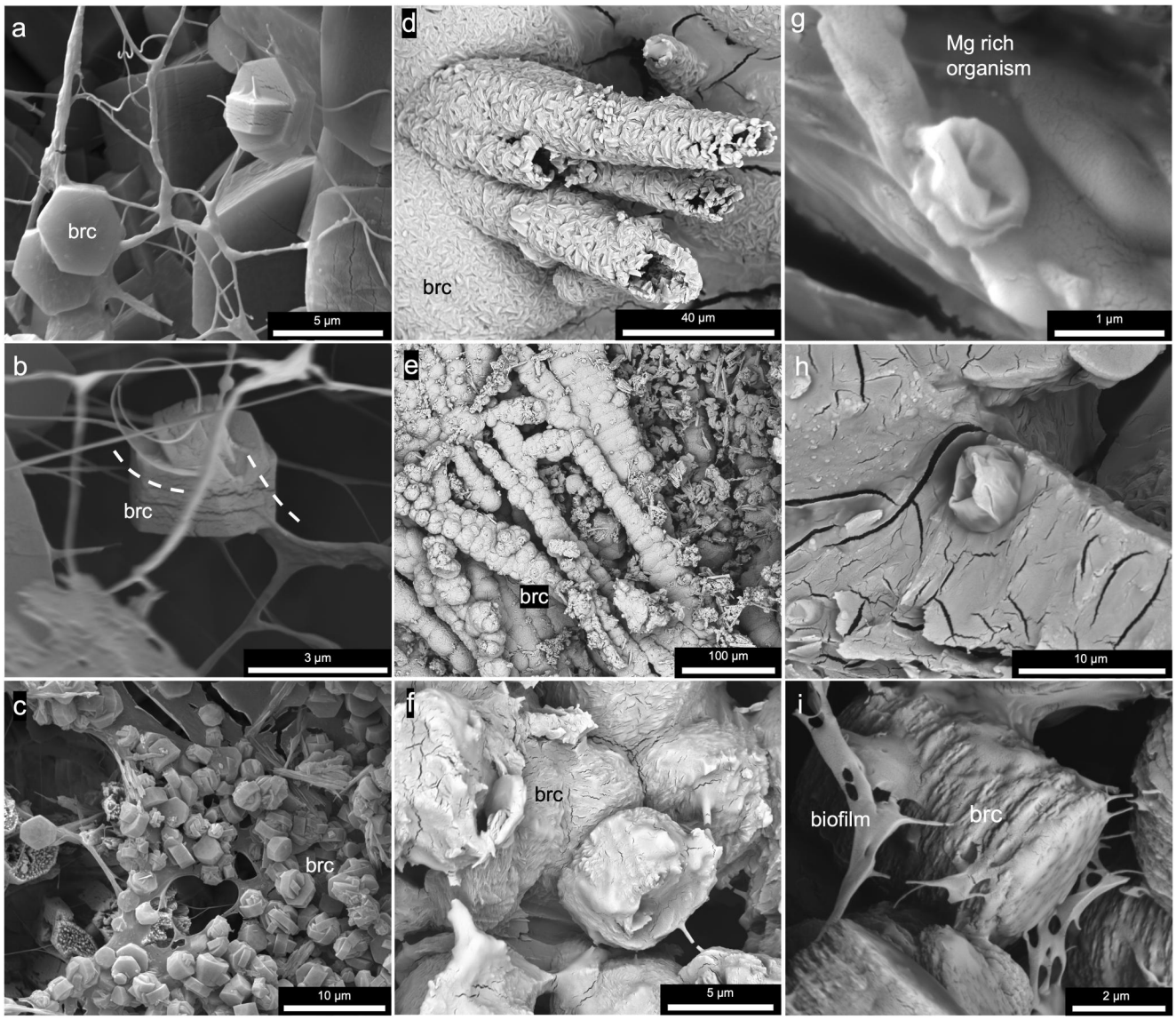


**Figure 9.** Examples of brucite-biofilm association in Marker C. (a) Hexagonal brucite plates on a network of microbial filaments. (b) The basal plane of brucite crystals is oriented parallel to microbial filaments. (c) Brucite crystals that precipitated on a biofilm. (d) Mineralized organism partly buried in botryoidal brucite. (e) Chains of brucite spheres likely formed from the mineralization of microbial filaments. (f) Putative partly mineralized microorganism. (g) Putative permineralized microorganism enveloped by a Mg-rich biofilm. (h) Putative microbial cell partly buried in an Mg-rich biofilm. (i) Stack of brucite plates associated with a partially preserved matrix of extracellular polymeric substances.

honeycomb- and parachute-like structures (Table S3 in Supporting Information S1; Figures 9 and 10). EPS is a matrix of various polymers including polysaccharides, proteins, nucleic acids, and lipids produced by microorganisms and serves as their immediate environment (Flemming & Wingender, 2010). The presence of biofilms/EPS is heterogenous even within the same sample and interestingly, they are most commonly associated with brucite. In addition to brucite within the chimney matrix acting as a substrate for biofilms, we observed that individual crystals of brucite may precipitate directly on the microbial filaments or sheets (Figures 9a–9c). In some cases, the microbial filaments seem to influence the growth direction of brucite crystals (Figure 9b). We also observed microbial filaments or worm-like microorganisms that appear to have been partly to fully mineralized by brucite or covered by a Mg-rich thin film (Figures 9d–9h). Microbial biofilms holding together stacks of brucite plates in Marker C were also detected (Figure 9i). In one sample from Sombrero (LC01370B), instead of brucite, microbial biofilms are associated with an Mg-silicate phase of undeterminable composition and structure

(Figure 10a; Figure S8 in Supporting Information S1). Unfortunately, we were unable to conduct further analyses on this phase.

Interestingly, the intimate relationship of biofilms with these Mg-bearing phases (brucite, Mg silicate) is not observed with aragonite or calcite under the SEM. Even in places where biofilms are observed together with aragonite, direct precipitation of aragonite on the biofilms were not observed and the biofilms are simply draping over or covering aragonite (Figure 10b). It is important to note, however, that although our observations indicate a close association between brucite precipitation and microbial biofilms/filaments, brucite mostly precipitates in the absence of microbial biofilms and may nucleate upon previously formed minerals (Figures 10c and 10d).

Parachute-like structures, similar to those previously described in *Pseudomonas fluorescens* isolated from soil (Baum et al., 2009), were observed in some Lost City samples. This structure comprises a canopy of biofilm material that appears to be tethered to the minerals via one or two thin fibers (Figure 10e). Relatively large filamentous tube-like microorganisms greater than 100 μm long and about 20 μm in diameter were detected in troughs in between adjacent aragonite spherical aggregates of a sample from Marker C (LC01797A), while the aragonite themselves are covered by a thick layer of EPS (Figure 10f; Figure S2f in Supporting Information S1). These tube structures may also be completely mineralized by brucite. Although definite identification of these organisms is not possible with the methods used in our study, the morphology of these tubes is similar to the external structures of tube worms (Kupriyanova et al., 2011). In samples from Marker C and Marker 6, long filamentous C-rich organisms, about 200 and 1,000 μm long, respectively, are present (Figures 10g and 10h; Figure S8 in Supporting Information S1). In Marker 6, this organism is associated with an abundant biofilm characterized by a complex arrangement of fibrillary structures that grade into a semi-organized network of fibers forming honeycomb-like pore spaces (Figure 10i; Figure S8 in Supporting Information S1), which is a common EPS microstructure observed in biofilms and microbial mats in sedimentary environments (Bontognali et al., 2008; Schaudinn et al., 2007).

Fluorescence microscopy shows that the brucite mineral membranes described above are more fluorescent than the carbonates (Figure 11), with the difference more pronounced in samples associated with biofilms (e.g., Calypso) than in those where no biofilms were observed (e.g., Beehive, Figures S3j–S3k in Supporting Information S1). Interestingly, we observed a rough correlation between brucite fluorescence and crystallinity: fluorescent brucite from Calypso displayed lower crystallinity than that from Beehive (Figure 12). Brucite from Marker C, which is also associated with microbial biofilms (Figure 9), has relatively lower crystallinity (Figure 12). However, we would like to point out that the x-ray diffraction data on which the crystallinity calculations are based are obtained from bulk samples, whereas the occurrence of biofilms and the occurrence of highly fluorescent brucite is only locally observed.

We also observed fluorescent filamentous structures within the channels. These structures are reminiscent of microbial filaments similar to those observed with SEM (Figures 11e and 11f). Micro-CT analyses confirm the presence of these low-density filamentous strands within the chimney conduits (Figure 6b; Figure S13 in Supporting Information S1). These low-density filaments are sometimes associated with a rhombohedral, high-density mineral, which may be calcite based on the form and density (Figure S13 in Supporting Information S1).

## 5. Discussion

### 5.1. Controls on the Variations in Mineralogy

Our results show clear differences in the mineralogy between the interior and exterior of hydrothermal chimneys and flanges in Lost City. Previous investigations of samples collected across a basal transect of a chimney near Marker H revealed a similar systematic difference in both mineralogy and geochemistry of the interior versus the rim of the sample (Figure S14 in Supporting Information S1) (Ludwig et al., 2006, 2011; Vogel, 2016). Although the results of previous studies emphasized the large variability within a single sample (Ludwig et al., 2006, 2011; Vogel, 2016), and even alluded that heterogenous precipitation conditions such as variable temperature and pH may result in the observed mineralogical and geochemical heterogeneity (Schmid, 2011), a mechanistic explanation is lacking.

In our companion paper (Aquino et al., 2024), we present geochemical data ($\delta^{13}C$, $\delta^{18}O$, $\Delta_{47}$, and $^{87}Sr/^{86}Sr$) of the Lost City chimneys that constrain the impact of fluid geochemistry on mineralogy and the geochemistry of the precipitating minerals. We suggest that variable mixing ratios between seawater and hydrothermal fluids control

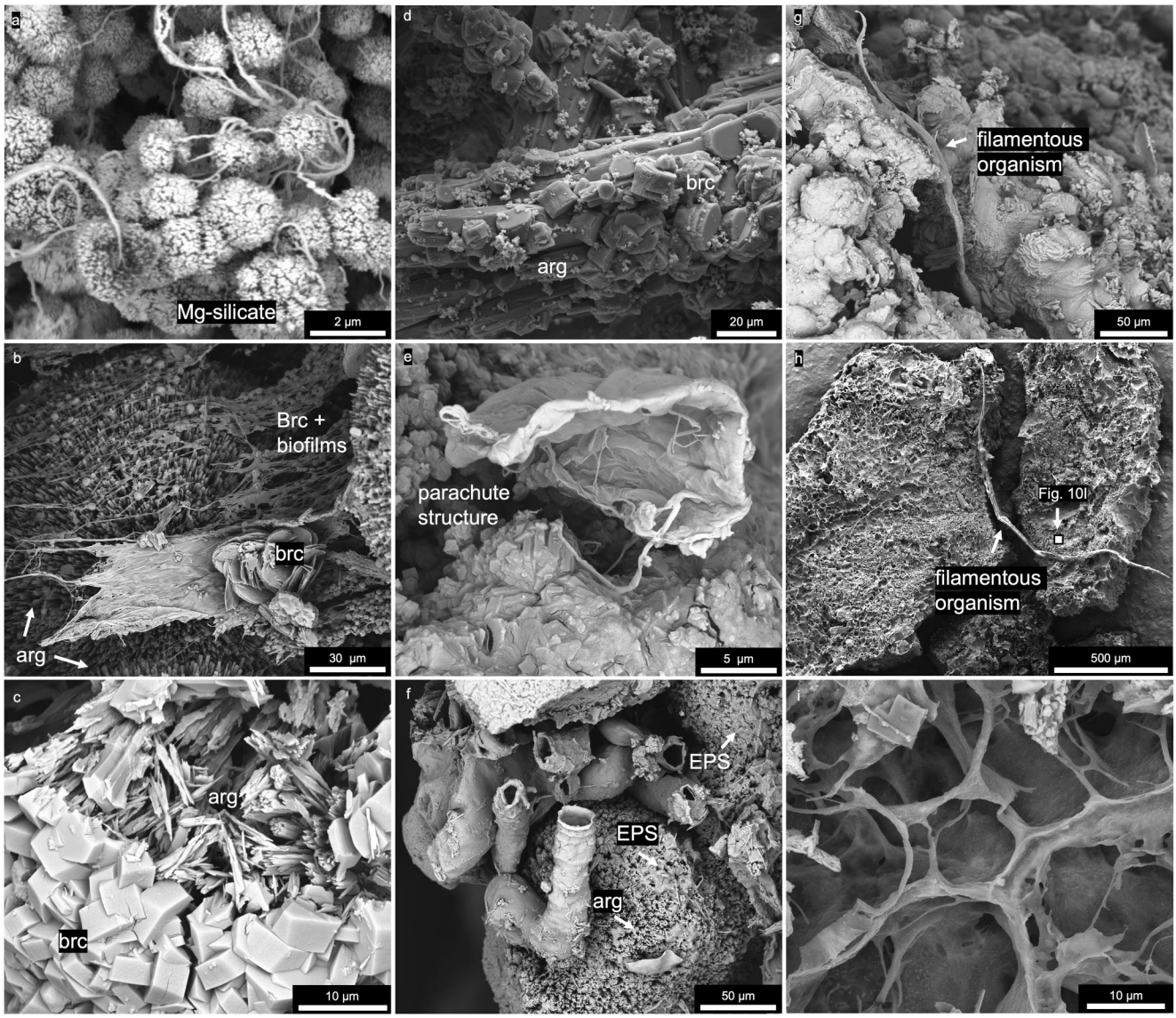


**Figure 10.** Biofilm occurrence in Lost City chimneys. (a) Mg-silicate phase that precipitated on microbial biofilms in Sombrero. (b) In Marker C, biofilm is associated with both aragonite and brucite, but only brucite is observed to precipitate directly on the biofilm. The biofilm covers or drapes over the aragonite. (c, d) Brucite precipitating on earlier formed aragonite in (c) Marker C and (d) Marker 8. (e) Parachute-like structures in Marker 8 consisting of a canopy of biofilm material tethered by a thin fibril structure. (f) Tube like organisms living in between adjacent aragonite spheres in Marker C. (g, h) Long filamentous structures in (g) Marker C and (h) Marker 6. (i) Biofilm in Marker 6 occurs as a network of fibers that in some places form honeycomb-like textures.

fluid geochemistry (e.g., Mg/Ca), and in turn affect the mineralogy and geochemistry of the precipitating minerals. The endmember vent fluids at Lost City are alkaline (pH 9–11), have little to no Mg, and are rich in Ca (Aquino et al., 2022; Kelley et al., 2005; Lang et al., 2012). Thus, the interiors of the chimneys are bathed in a vent-fluid dominated solution characterized by higher pH and lower Mg/Ca ratios. These conditions promote the precipitation of calcite and brucite. In contrast, aragonite precipitates in the chimney exterior, reflecting an increase in Mg/Ca and decrease in pH resulting from a larger contribution of seawater. We also show that calcite records relatively higher clumped ($\Delta_{47}$) and oxygen ($\delta^{18}O$) isotope temperatures and lower $^{87}Sr/^{86}Sr$ than aragonite, in concert with its precipitation from a higher temperature vent fluid-rich solution. At lower temperatures, the threshold Mg/Ca ratio for aragonite precipitation is higher, favoring calcite precipitation at a wider range of seawater and hydrothermal fluid mixing ratios (Aquino et al., 2024). This may explain why samples from the lower temperature sites such as in Calypso, and some of the carbonate veins have relatively high amounts of calcite (Figure 3; Figures S1e and S1f in Supporting Information S1). In sample 3881–1338, the interior (transect

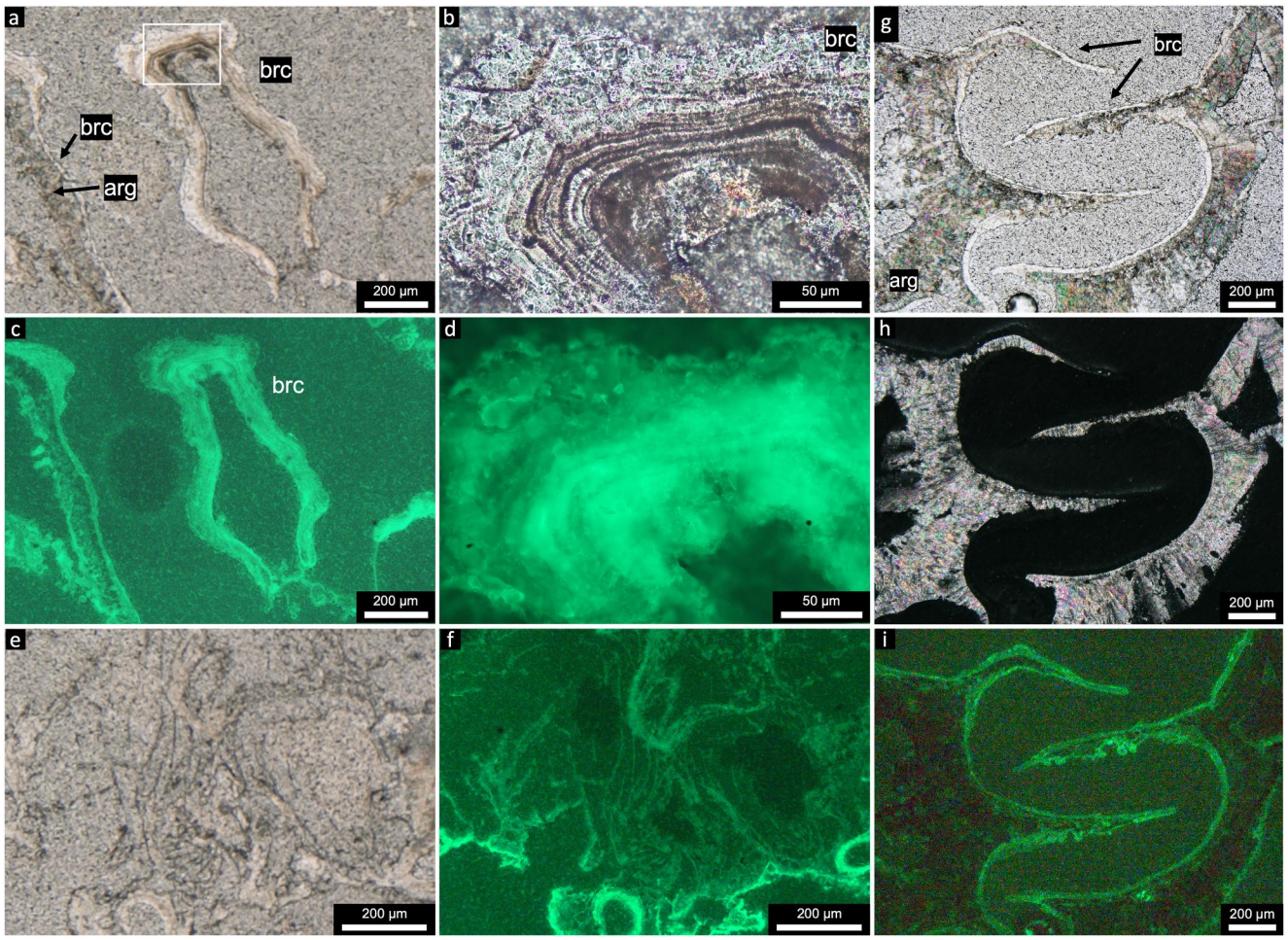


**Figure 11.** Conventional and fluorescence microscopy images of sample 1108–2002 from Calypso. (a) The mineral membrane is composed of brucite on which later-formed aragonite may precipitate. (b) Detail of white box on B showing brown laminations in the brucite membrane. (c) Fluorescence microscopy image of a showing that brucite is more fluorescent than aragonite. (d) Fluorescence microscopy image of b showing strong fluorescence in brucite, especially on the brown laminations. (e, f) Fluorescent filamentous material. (g) Channel flow structure bounded by mineral membranes made up of brucite and aragonite. Brucite lines the interior of the channel. Image taken in plane polarized light. (h) Same as g in crossed polarized light. Aragonite exhibits strong birefringence while brucite has low to anomalous interference colors. (i) Fluorescence microscopy image of (g, h). Brucite, which lines the channel, is more fluorescent than aragonite.

no. 2 and 3) is composed of calcite and brucite and has a higher precipitation temperature and lower Mg/Ca than the aragonite-bearing exterior, consistent with our interpretation (Figure S14 and Table S4 in Supporting Information S1).

Multiple lines of evidence point to the existence of primary calcite in the chimneys and veins, including its higher precipitation temperatures (Aquino et al., 2024), Mg/Ca ratios that favor calcite over aragonite precipitation, and the close association of calcite and brucite in the chimney interiors (Figure 8). Consistent with this interpretation, primary calcite has lower $^{87}Sr/^{86}Sr$ ratios relative to aragonite and inactive chimney samples, reflecting the formation from fluids that have relatively less seawater contribution (Aquino et al., 2024). Secondary calcite, on the other hand, is formed from the alteration of aragonite and occurs in inactive or extinct samples that have been weathered by seawater (Ludwig et al., 2006). These older samples often have little to no brucite.

Like the chimneys, the hydrothermal veins are also composed of variable mixtures of aragonite, calcite, and brucite. These hydrothermal veins were formed by hydrothermal fluids flowing in the fracture network in the shallow subsurface of the Atlantis Massif (Ludwig et al., 2006). The interior of the veins contains similar or slightly more brucite than the exterior (Figures 3 and 4), suggesting a comparable spatial control as in the chimneys, albeit to a lesser degree. In contrast to the fissure deposits collected within the LCHF, carbonate veins recovered from drilling the shallow basement of the Atlantis Massif do not contain brucite (Ternieten

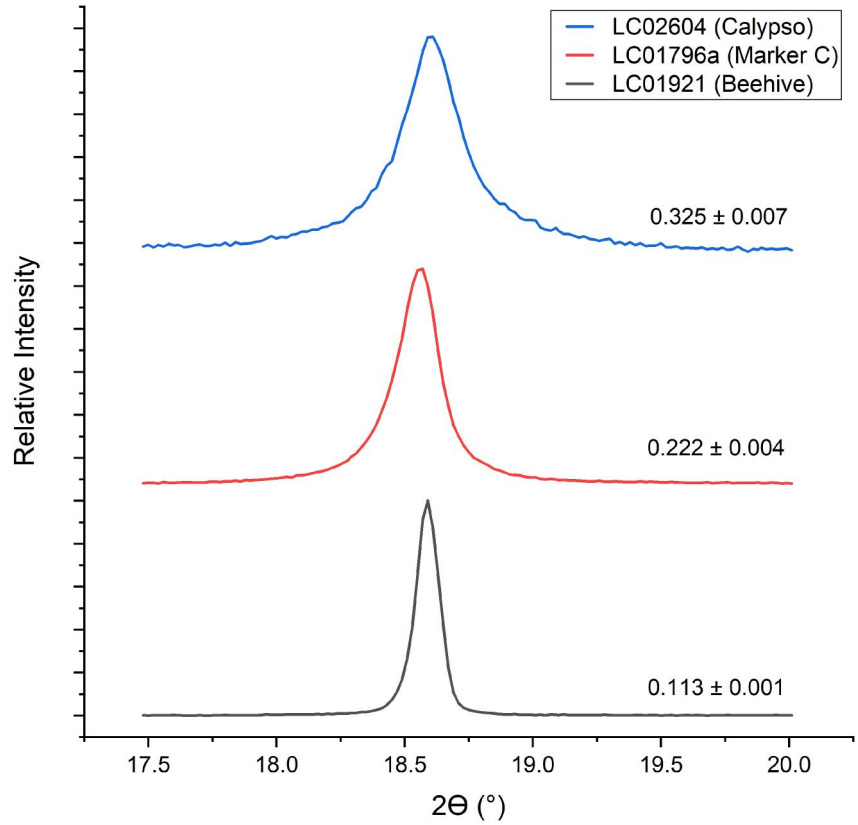


**Figure 12.** Crystallinity of brucite in representative Lost City chimney samples. The crystallinity is estimated by performing a Gaussian fit of the X-ray diffraction data and calculating the full-width at half maximum (FWHM) of the brucite (001) peak (FWMH values are shown). Brucite from Beehive is relatively more crystalline (lower FWHM) than those from Calypso and Marker C, where abundant microbial biofilms are observed.

et al., 2021a). Similar to the chimneys, the $^{87}Sr/^{86}Sr$ compositions of the veins indicate that they form from a mixture of seawater and hydrothermal fluids (Aquino et al., 2024). The veins also contain relatively more calcite than the chimneys (Figure 3; Figures S1e and S1f in Supporting Information S1). $\delta^{18}O$ and $\Delta_{47}$ data suggest that the veins we investigated in this study are formed at lower temperatures (<10°C). As mentioned above, at lower temperatures, the threshold Mg/Ca ratio for aragonite precipitation is higher, favoring calcite precipitation at a wider range of seawater and hydrothermal fluid mixing ratios (Aquino et al., 2024). Together, these data highlight the importance of near-surface mixing of seawater in the development of Lost City veins.

### 5.2. Channel Wall Development

Most of the samples we investigated preserve channel flow structures that are bounded by mineral membranes. These mineral membranes serve as the backbone of the structure of most chimneys and veins and may be preserved as venting wanes and ceases (Figure 7). In young active chimneys, mineral channel walls are made up of brucite, which is stable at relatively higher pH (Pokrovsky & Schott, 2004) and precipitates from solutions dominated by vent fluids (Figure 13a; Aquino et al., 2024). The carbonate mineral that precipitates depends on the Mg/Ca of the fluid, which is controlled by the extent of vent fluid-seawater mixing (see Section 5.1). Later renewed influx of vent fluid results in the precipitation of brucite on the previously formed aragonite (Figure 13b).

In mature, yet still active hydrothermal chimneys, earlier formed minerals that comprise the channel walls are fused together to form distinct brucite and aragonite layers (Figure 13c; Figures S4g and S9b in Supporting Information S1), with the original mineral crystal faces unrecognizable. Brucite and carbonate precipitation within the channels continue depending on the nature of the mixed fluid (see Section 5.1). In channels where vent fluid is the dominant component, aggregates of brucite and calcite form (Figures 8 and 13c). Where seawater is dominant, aragonite precipitates perpendicular to the channel walls (Figure 13c; Figures S4a–S4d in Supporting

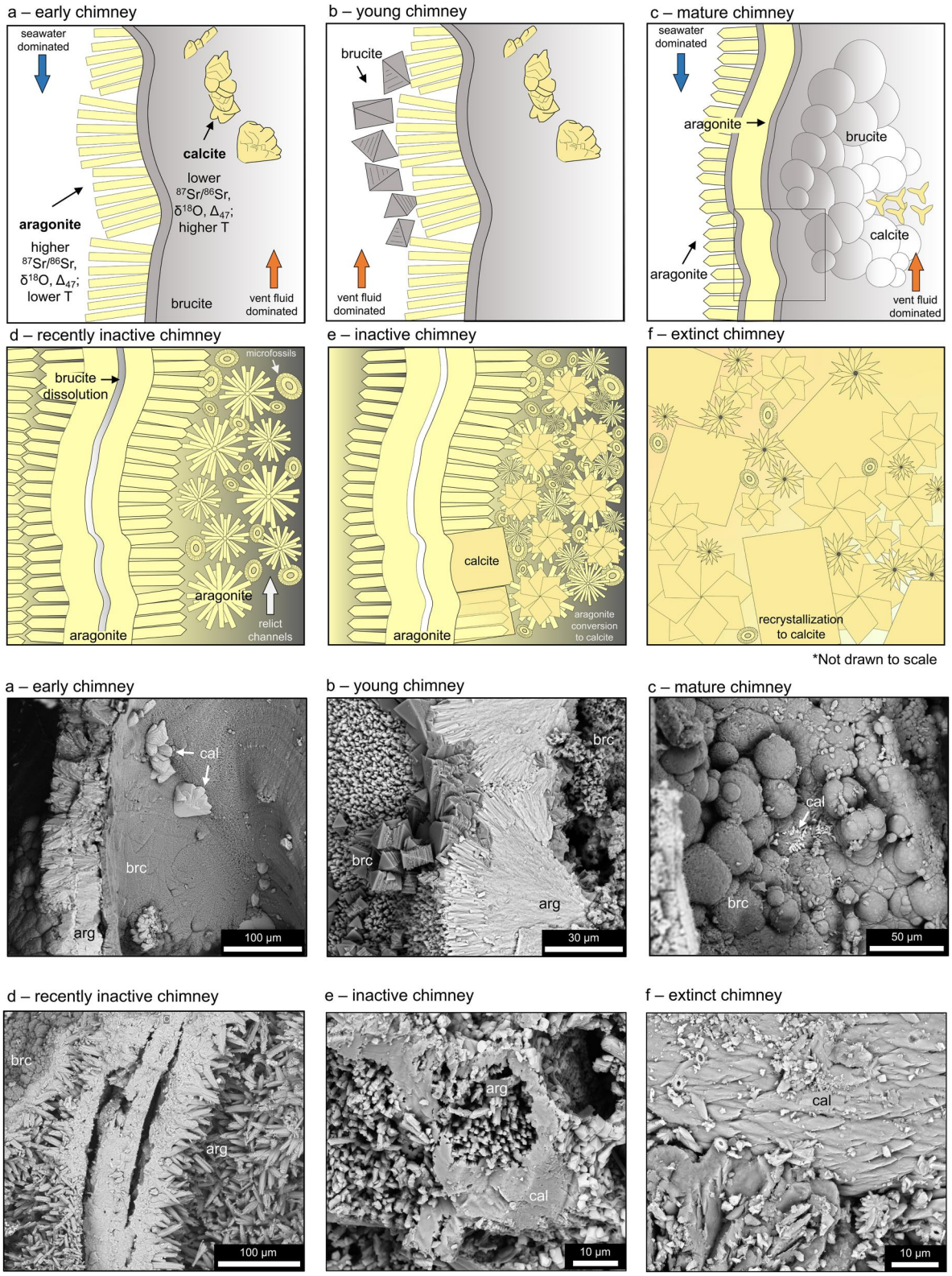


**Figure 13.**

Information S1). In mature chimneys, channel walls thicken from multiple venting events that form alternating layers of aragonite and brucite (Figure 13c). Minor brucite dissolution may occur locally (Figure S4c in Supporting Information S1). However, brucite precipitation is more prevalent.

Chimney structures become inactive when focused hydrothermal fluid flow wanes. Brucite is unstable at seawater pH and slowly dissolves leaving a chimney composed mostly of carbonates (Figures 13d and 13e; Figures S9–S12 in Supporting Information S1). Mineral channel wall structures are preserved as aragonite and occasional microfossils are found within the channels (Figures 13d and 13e; Figures S9 and S10 in Supporting Information S1). Initial alteration of aragonite to calcite may occur (Figure 13e; Figures S10a–S10d in Supporting Information S1). Prolonged exposure of the chimney to seawater (>5,000 years, Table 1) results in the continued conversion of aragonite to calcite (Figures S10e–S10h in Supporting Information S1). Aragonite channel walls are still recognizable, and the previously formed fluid flow channels are increasingly filled by microcrystalline calcite (Figure S11 in Supporting Information S1). Extinct chimneys are structures that have been inactive and bathed in seawater for more than tens of thousands of years (Früh-Green et al., 2003; Ludwig et al., 2006). In extinct structures, channels are no longer discernible (Figures 7d and 13f). Aragonite has been completely recrystallized into calcite. The channels are filled by micritic calcite and micro- and nanofossils, producing a massive dense structure (Figures S12 in Supporting Information S1; Figure 7d).

### 5.3. Biotic and Abiotic Controls on Brucite Precipitation

Brucite is a significant component of young active Lost City chimneys, especially within their vent fluid-bathed interior (Figures 3 and 4). In our companion paper (Aquino et al., 2024), we show that mixing between end-member Beehive vent fluids and small amounts of seawater (up to ∼30 wt %) results in the precipitation of brucite, highlighting that at least for Beehive, most brucite precipitation may occur readily simply inorganically by supersaturation induced by mixing. This is also consistent with the occurrence of brucite in the vent-fluid dominated interior of the chimneys. In addition, our textural investigation suggests an important connection between microbial biofilms and brucite that is not observed with the carbonate minerals (Section 4.5).

One possibility is that the brucite mineral surfaces provide a substrate that is more favorable for the formation of biofilms by the microorganisms than the carbonates, leading to preferential growth of biomass along the brucite channel walls (e.g., Hutchens, 2009). Previous studies highlighting the adsorption of organic matter on brucite mineral surfaces may support this hypothesis. For example, Wang et al. (2017) used in situ atomic force microscopy to directly observe the contribution of brucite surface dissolution to the supersaturation, nucleation, and growth of Mg-organophosphate/pyrophosphate on the brucite (001) surface. Batch adsorption experiments of Estrada et al. (2015), on the other hand, revealed that $Ca^{2+}$ ions may promote aspartate adsorption on brucite, while $Mg^{2+}$ ions may limit this interaction. This observation is highly relevant to our results as the co-occurrence of brucite and organic matter is typically observed in chimney interiors bathed in Ca-rich and Mg-poor vent fluids (Kelley et al., 2005; Seyfried et al., 2015).

In addition, microbial EPS may promote the precipitation of brucite by acting as a physical substrate for mineral nucleation. In general, microbes may play a role in the precipitation of minerals via microbially controlled, microbially induced, and microbially influenced processes, collectively known as organomineralization (see review by Dupraz et al., 2009; Cosmidis & Benzerara, 2022). In microbially controlled mineralization, the microbes play an active role in the mineral precipitation, where the nucleation, growth, morphology, and location of the minerals are directed by microbial activity. On the other hand, in microbially induced mineralization

**Figure 13.** Conceptual model of channel wall development in active and inactive chimneys. (a) Initially, chimneys are characterized by brucite mineral membranes that precipitate from a vent-fluid dominated solution. These brucite layers bound fluid flow paths and form an interconnected network of cavities. As more seawater rapidly mixes with the fluids, later formed minerals precipitate on these channel walls, with the mineralogy dictated by the fluid composition (i.e., vent fluid vs. seawater dominated, see Aquino et al., 2024 for details). (b) Precipitation of brucite on earlier formed aragonite or continued aragonite precipitation occurs as a result of numerous venting events and mixing with seawater. (c) In mature chimneys, earlier formed minerals fuse together, and the crystal boundaries are no longer clear. Within the channels, extensive precipitation of botryoidal aggregates of minerals occurs. Like in young chimneys, the mineralogy depends on the degree of vent fluid and seawater mixing. Brucite and calcite precipitates from a vent fluid-dominated solution and aragonite from a seawater-dominated fluid. Box shows the approximate area drawn in (a, b). (d) As hydrothermal venting wanes, brucite is no longer stable and starts to dissolve. Only aragonite precipitation from a seawater-dominated fluid occurs. Occasional microfossils are deposited within the channels. (e) In an inactive chimney, most of the brucite is dissolved. The initial alteration of aragonite to calcite may occur within as little as 1,000 years after inactivity. Microfossils continue to be deposited within pore spaces. (f) Continued reaction to seawater results in recrystallization of aragonite to calcite in an extinct chimney. Note: The last two rows represent the corresponding scanning electron images.

processes, microbial activity and its interaction with the environment lead to mineral precipitation. Lastly, microbially influenced mineralization is simply the passive precipitation of minerals on organic matter. Here, the precipitation may result from other external environmental factors and is not a direct result of microbial activities. The presence of living organisms is not required. There is evidence for biologically influenced mineralization at Lost City. Brucite (and Mg silicate) was observed to precipitate directly on microbial filaments, on EPS, as well as on the surfaces of organisms (Figures 9 and 10). Our results suggest that the orientation of the crystal growth of brucite crystals may be influenced by the biofilm (Figure 9b). In some samples, although the presence of EPS is not apparent, EDX analyses indicate small amounts of C despite the absence of $CaCO_3$ (i.e., little or no Ca detected) (Figure S13 in Supporting Information S1). The higher fluorescence exhibited by brucite relative to the carbonates also points to the presence of fluorescent organic matter in brucite (Figure 11). Authigenic Mg-rich silicates with similar morphologies as those in the Lost City samples have previously been observed locally in biofilms in evaporites and are interpreted as the result of progressive mineralization of microstructures comprised of EPS (Bontognali et al., 2010). Brucite biomineralization on hydrothermally derived microbial filaments has also been reported at the Prony Bay hydrothermal field (New Caledonia), especially at the most juvenile hydrothermal chimneys (Pisapia et al., 2017). These authors hypothesized that the microbes may have been important in the early construction of the chimneys.

In addition to precipitation where organic matter serves as a physical template for mineral nucleation, microbial EPS could also contribute locally to brucite supersaturation by recycling and concentrating seawater Mg. EPS can bind cations (e.g., Ca, Mg) depending on the pH and the functional groups involved (Braissant et al., 2007; Phoenix et al., 2002; Sokolov et al., 2001). These cations may be released during EPS degradation (due to dehydration, pH changes, organic carbon oxidation), increasing mineral saturation (Dupraz et al., 2009). Let us take for example, a hypothetical spherical cavity with a 1 mm radius. If the internal surface area of this sphere is covered with a 10 μm-thick EPS layer, which corresponds to a volume of $1.26 \times 10^{-7}$ L or 0.126 $mm^3$, $3.14 \times 10^{-8}$ mmol of cations may bind to this EPS assuming a cation binding capacity of 0.25 mM (Braissant et al., 2007). If these cation binding sites are filled with Mg, and if the cavity has the appropriate pH, more than 27,000 small brucite crystals, about 3 μm × 3 μm × 1 μm such as those seen in Figure 9a, may precipitate in this cavity. However, future work, including EPS functional group characterization and proton-binding experiments (e.g., Braissant et al., 2007; Phoenix et al., 2002), is necessary to better understand the dynamics of biomineralization at the Lost City chimneys.

At Lost City, the internal structure of hydrothermal chimneys comprises brucite-carbonate mineral membranes forming a network of cavities (see Section 4.1; Ludwig et al., 2006). These mineral membranes may act as a barrier separating a reduced, electron-rich interior from an oxidized external environment (Duval et al., 2019; Russell, 2018). Templeton and Ellison (2020) discussed the role that Fe-brucite plays as a reactive electron donor that may serve as a metabolic substrate for microbial organisms in serpentinizing environments. Accumulations of microbial lipids were also detected in hydrothermal brucite from the Iberian Margin and at the Chimaera seeps in Turkey (Klein et al., 2015; Zwicker et al., 2018). Lastly, microbially influenced mineralization on microbial filaments, very similar to that described here, has been reported at the Prony Bay hydrothermal field in New Caledonia (Pisapia et al., 2017). Clearly, the relationship between organic matter and brucite is a common theme in AHVs. The possibility that the biofilm is not simply a passive substrate for mineral nucleation and the organic ligands may play an active role in the recycling of seawater Mg, at least locally, opens interesting questions regarding the ecological significance of this mineral-microbe interaction. Do microbes draw any advantage through the precipitation of brucite? As described above, future work including EPS characterization and/or mineral precipitation experiments in the presence of Lost City EPS are steps that may help address these unresolved questions.

## 6. Conclusions

In this paper, we describe the mineralogy and textures of hydrothermal chimneys from Lost City and document the intimate association between brucite and microbial biofilms. Flow textures in the chimneys are mostly preserved as brucite-carbonate channel walls that bound paleo-fluid flow paths. Brucite typically precipitates in the interior of the chimneys and in the inner lining of these channels and is locally associated with primary calcite. Aragonite, on the other hand, precipitates on the exterior. In young active chimneys, mineral channel walls are initially composed of brucite, upon which later precipitation of carbonate and/or brucite minerals may occur. These channel walls are preserved to varying degrees in samples from inactive vents. Fluorescence microscopy of

these channel walls pointed to the presence of fluorescent organic compounds associated with brucite but not with the carbonate minerals. We suggest that microbial sheaths, filaments, and EPS found within these channels influence the morphology of brucite and serve as substrates for further brucite precipitation or provide a better substrate than calcite for the formation of biofilms. There is also a possibility that microbes may play a more active role in recycling seawater-derived Mg and $OH^-$ within the chimney cavities and may contribute to brucite precipitation, at least locally. Further work, including characterization of microbial EPS is necessary to test this hypothesis. At Lost City, mineral bound channel walls may create micro-compartments characterized by ideal conditions (temperature, pH), protected from external environmental factors, where microorganisms may live and survive. Indeed, abundant microbes inhabiting these channels may aid brucite mineralization.

## Data Availability Statement

Individual analyses and raw microscopy images are available at the ETH Research Collection (Aquino, 2022).

**Acknowledgments**
We thank the captain and crew of the R/V Atlantis, ROV Jason, and the scientific party of the 2018 expedition AT42-01. Funding was provided by NSF awards OCE-1536702/1536405/1535962, the Swiss National Science Foundation project No. 200021_163187, the Joint Institute for the Study of the Atmosphere and Ocean (JISAO) under NOAA Cooperative Agreement NA15OAR4320063—Contribution No. 2021-1132, the Deep Carbon Observatory, and the Philippine Department of Science and Technology–Science Education Institute (DOST-SEI). We thank Luiz Morales for assistance with the SEM analyses, Christoph Neururer for the micro-CT analyses, and Negar Haghipour for the radiocarbon analyses. We appreciate the thoughtful reviews of D. Foustoukos and B. Tutolo, who helped to improve this manuscript.

## References

Allen, D. E., & Seyfried, W. E. (2004). Serpentinization and heat generation: Constraints from Lost City and rainbow hydrothermal systems. *Geochimica et Cosmochimica Acta*, *68*(6), 1347–1354. https://doi.org/10.1016/j.gca.2003.09.003

Alt, J. C. (1995). Sulfur isotopic profile through the oceanic crust: Sulfur mobility and seawater-crustal sulfur exchange during hydrothermal alteration. *Geology*, *23*(7), 585–588. https://doi.org/10.1130/0091-7613(1995)023<0585:SIPTTO>2.3.CO;2

Aquino, K. A. (2022). Biotic and abiotic mineral formation at the Lost City hydrothermal field (Research data) [Dataset]. Research Collection. https://doi.org/10.3929/ethz-b-000579718

Aquino, K. A., Früh-Green, G. K., Bernasconi, S. M., Rickli, J., Lang, S. Q., & Lilley, M. D. (2024). Fluid mixing and spatial geochemical variability in the Lost City hydrothermal field chimneys. *Geochemistry, Geophysics, Geosystems*, *25*, e2023GC011011. https://doi.org/10.1029/2023GC011011

Aquino, K. A., Früh-Green, G. L., Rickli, J., Bernasconi, S. M., Lang, S. Q., Lilley, M. D., & Butterfield, D. A. (2022). Multi-stage evolution of the Lost City hydrothermal vent fluids. *Geochimica et Cosmochimica Acta*, *332*, 239–262. https://doi.org/10.1016/j.gca.2022.06.027

Baum, M. M., Kainović, A., O'Keeffe, T., Pandita, R., McDonald, K., Wu, S., & Webster, P. (2009). Characterization of structures in biofilms formed by a Pseudomonas fluorescens isolated from soil. *BMC Microbiology*, *9*, 1–13. https://doi.org/10.1186/1471-2180-9-103

Blackmann, D. K., Karson, J. A., Kelley, D. S., Cann, J. R., Früh-Green, G. L., Gee, J. S., et al. (2002). Geology of the Atlantis Massif (Mid-Atlantic Ridge, 30°N): Implications for the evolution of an ultramafic oceanic core complex. *Marine Geophysical Researches*, *23*(5–6), 443–469. https://doi.org/10.1023/b:mari.0000018232.14085.75

Bontognali, T. R. R., Vasconcelos, C., Warthmann, R. J., Bernasconi, S. M., Dupraz, C., Strohmenger, C. J., & Mckenzie, J. A. (2010). Dolomite formation within microbial mats in the coastal sabkha of Abu Dhabi (United Arab Emirates). *Sedimentology*, *57*(3), 824–844. https://doi.org/10.1111/j.1365-3091.2009.01121.x

Bontognali, T. R. R., Vasconcelos, C., Warthmann, R. J., Dupraz, C., Bernasconi, S. M., & McKenzie, J. A. (2008). Microbes produce nanobacteria-like structures, avoiding cell entombment. *Geology*, *36*(8), 663–666. https://doi.org/10.1130/G24755A.1

Braissant, O., Decho, A. W., Dupraz, C., Glunk, C., Przekop, K. M., & Visscher, P. T. (2007). Exopolymeric substances of sulfate-reducing bacteria: Interactions with calcium at alkaline pH and implication for formation of carbonate minerals. *Geobiology*, *5*(4), 401–411. https://doi.org/10.1111/j.1472-4669.2007.00117.x

Brazelton, W. J., McGonigle, J. M., Motamedi, S., Pendleton, H. L., Twing, K. I., Miller, B. C., et al. (2022). Metabolic strategies shared by basement residents of the Lost City hydrothermal field. *Applied and Environmental Microbiology*, *88*(17). https://doi.org/10.1128/aem.00929-22

Brazelton, W. J., Schrenk, M. O., Kelley, D. S., & Baross, J. A. (2006). Methane- and sulfur-metabolizing microbial communities dominate the lost city hydrothermal field ecosystem. *Applied and Environmental Microbiology*, *72*(9), 6257–6270. https://doi.org/10.1128/AEM.00574-06

Cosmidis, J., & Benzerara, K. (2022). Why do microbes make minerals? *Comptes Rendus Geoscience*, *354*(1), 1–39. https://doi.org/10.5802/CRGEOS.107

Dupraz, C., Reid, R. P., Braissant, O., Decho, A. W., Norman, R. S., & Visscher, P. T. (2009). Processes of carbonate precipitation in modern microbial mats. *Earth-Science Reviews*, *96*(3), 141–162. https://doi.org/10.1016/j.earscirev.2008.10.005

Duval, S., Baymann, F., Schoepp-Cothenet, B., Trolard, F., Bourrié, G., Grauby, O., et al. (2019). Fougerite: The not so simple progenitor of the first cells. *Interface Focus*, *9*(6), 16–20. https://doi.org/10.1098/rsfs.2019.0063

Estrada, C. F., Sverjensky, D. A., Pelletier, M., Razafitianamaharavo, A., & Hazen, R. M. (2015). Interaction between l-aspartate and the brucite [Mg(OH)2]–water interface. *Geochimica et Cosmochimica Acta*, *155*(155), 172–186. https://doi.org/10.1016/j.gca.2015.02.002

Flemming, H. C., & Wingender, J. (2010). The biofilm matrix. *Nature Reviews Microbiology*, *8*(9), 623–633. https://doi.org/10.1038/nrmicro2415

Foustoukos, D. I., Savov, I. P., & Janecky, D. R. (2008). Chemical and isotopic constraints on water/rock interactions at the Lost City hydrothermal field, 30°N Mid-Atlantic Ridge. *Geochimica et Cosmochimica Acta*, *72*(22), 5457–5474. https://doi.org/10.1016/j.gca.2008.07.035

Früh-Green, G. L., Kelley, D. S., Bernasconi, S. M., Karson, J. A., Ludwig, K. A., Butterfield, D. A., et al. (2003). 30,000 years of hydrothermal vent field. *Science*, *301*(July), 495–498. https://doi.org/10.1126/science.1085582

Früh-Green, G. L., Kelley, D. S., Lilley, M. D., Cannat, M., Chavagnac, V., & Baross, J. A. (2022). Diversity of magmatism, hydrothermal processes and microbial interactions at mid-ocean ridges. *Nature Reviews Earth & Environment*, *3*(12), 852–871. https://doi.org/10.1038/s43017-022-00364-y

German, C. R., & Von Damm, K. L. (2003). Hydrothermal processes. In *Treatise on geochemistry* (pp. 181–222). Elsevier. https://doi.org/10.1016/B0-08-043751-6/06109-0

Humphris, S. E., Zierenberg, R. A., Mullineaux, L. S., & Thomson, R. E. (1995). *Seafloor hydrothermal systems: Physical, chemical, biological, and geological interactions*. American Geophysical Union. https://doi.org/10.1029/GM091

Hutchens, E. (2009). Microbial selectivity on mineral surfaces: Possible implications for weathering processes. *Fungal Biology Reviews*, *23*(4), 115–121. https://doi.org/10.1016/j.fbr.2009.10.002

Karson, J. A., Früh-Green, G. L., Kelley, D. S., Williams, E. A., Yoerger, D. R., & Jakuba, M. (2006). Detachment shear zone of the Atlantis Massif core complex, Mid-Atlantic Ridge, 30°N. *Geochemistry, Geophysics, Geosystems*, *7*(6), Q06016. https://doi.org/10.1029/2005GC001109

Kelley, D. S., Karson, J. A., Blackman, D. K., Früh-Green, G. L., Butterfield, D. A., Lilley, M. D., et al. (2001). An off-axis hydrothermal vent field near the Mid-Atlantic Ridge at 30°N. *Nature*, *412*(6843), 145–149. https://doi.org/10.1038/35084000

Kelley, D. S., Karson, J. A., Früh-Green, G. L., Yoerger, D. R., Shank, T. M., Butterfield, D. A., et al. (2005). A serpentinite-hosted ecosystem: The Lost City hydrothermal field. *Science*, *307*(5714), 1428–1434. https://doi.org/10.1126/science.1102556

Klein, F., Humphris, S. E., Guo, W., Schubotz, F., Schwarzenbach, E. M., Orsi, W. D., & Karl, D. M. (2015). Fluid mixing and the deep biosphere of a fossil Lost City-type hydrothermal system at the Iberia Margin. *Proceedings of the National Academy of Sciences of the United States of America*, *112*(39), 12036–12041. https://doi.org/10.1073/pnas.1504674112

Konn, C., Charlou, J. L., Donval, J. P., Holm, N. G., Dehairs, F., & Bouillon, S. (2009). Hydrocarbons and oxidized organic compounds in hydrothermal fluids from Rainbow and Lost City ultrama fi c-hosted vents. *Chemical Geology*, *258*(3–4), 299–314. https://doi.org/10.1016/j.chemgeo.2008.10.034

Kupriyanova, E. K., Bailey-Brock, J., & Nishi, E. (2011). New records of serpulidae (Annelida, Polychaeta) collected by R/V "Vityaz" from bathyal and abyssal depths of the Pacific Ocean. *Zootaxa*, *2871*(2871), 43–60. https://doi.org/10.11646/zootaxa.2871.1.3

Lang, S. Q., & Brazelton, W. J. (2020). Habitability of the marine serpentinite subsurface: A case study of the Lost City hydrothermal field. *Philosophical Transactions of the Royal Society A: Mathematical, Physical & Engineering Sciences*, *378*(2165), 20180429. https://doi.org/10.1098/rsta.2018.0429

Lang, S. Q., Butterfield, D. A., Schulte, M., Kelley, D. S., & Lilley, M. D. (2010). Elevated concentrations of formate, acetate and dissolved organic carbon found at the Lost City hydrothermal field. *Geochimica et Cosmochimica Acta*, *74*(3), 941–952. https://doi.org/10.1016/j.gca.2009.10.045

Lang, S. Q., Früh-Green, G. L., Bernasconi, S. M., Brazelton, W. J., Schrenk, M. O., & McGonigle, J. M. (2018). Deeply-sourced formate fuels sulfate reducers but not methanogens at Lost City hydrothermal field. *Scientific Reports*, *8*(1), 1–10. https://doi.org/10.1038/s41598-017-19002-5

Lang, S. Q., Früh-Green, G. L., Bernasconi, S. M., Lilley, M. D., Proskurowski, G., Méhay, S., & Butterfield, D. A. (2012). Microbial utilization of abiogenic carbon and hydrogen in a serpentinite-hosted system. *Geochimica et Cosmochimica Acta*, *92*, 82–99. https://doi.org/10.1016/j.gca.2012.06.006

Ludwig, K. A., Kelley, D. S., Butterfield, D. A., Nelson, B. K., Früh-Green, G., Fru, G., & Früh-Green, G. (2006). Formation and evolution of carbonate chimneys at the Lost City hydrothermal field. *Geochimica et Cosmochimica Acta*, *70*(14), 3625–3645. https://doi.org/10.1016/j.gca.2006.04.016

Ludwig, K. A., Shen, C. C., Kelley, D. S., Cheng, H., & Edwards, R. L. (2011). U-Th systematics and 230 Th ages of carbonate chimneys at the Lost City Hydrothermal Field. *Geochimica et Cosmochimica Acta*, *75*(7), 1869–1888. https://doi.org/10.1016/j.gca.2011.01.008

Mcgonigle, J. M., Lang, S. Q., & Brazelton, W. J. (2020). Genomic evidence for formate metabolism by chloroflexi as the key to unlocking deep carbon in lost city microbial ecosystems. *Applied and Environmental Microbiology*, *86*(8), 1–12. https://doi.org/10.1128/AEM.02583-19

Phoenix, V. R., Martinez, R. E., Konhauser, K. O., & Ferris, F. G. (2002). Characterization and implications of the cell surface reactivity of Calothrix sp. strain KC97. *Applied and Environmental Microbiology*, *68*(10), 4827–4834. https://doi.org/10.1128/AEM.68.10.4827-4834.2002

Pisapia, C., Gérard, E., Gérard, M., Lecourt, L., Lang, S. Q., Pelletier, B., et al. (2017). Mineralizing filamentous bacteria from the prony bay hydrothermal field give new insights into the functioning of serpentinization-based subseafloor ecosystems. *Frontiers in Microbiology*, *8*(JAN), 1–18. https://doi.org/10.3389/fmicb.2017.00057

Pokrovsky, O. S., & Schott, J. (2004). Experimental study of brucite dissolution and precipitation in aqueous solutions: Surface speciation and chemical affinity control. *Geochimica et Cosmochimica Acta*, *68*(1), 31–45. https://doi.org/10.1016/S0016-7037(03)00238-2

Proskurowski, G., Lilley, M. D., Kelley, D. S., & Olson, E. J. (2006). Low temperature volatile production at the Lost City Hydrothermal Field, evidence from a hydrogen stable isotope geothermometer. *Chemical Geology*, *229*(4), 331–343. https://doi.org/10.1016/j.chemgeo.2005.11.005

Proskurowski, G., Lilley, M. D., Seewald, J. S., Früh-Green, G. L., Olson, E. J., Lupton, J. E., et al. (2008). Abiogenic hydrocarbon production at lost city hydrothermal field. *Science*, *319*(5863), 604–607. https://doi.org/10.1126/science.1151194

Reimer, P. J., Brown, T. A., & Reimer, R. W. (2004). Discussion: Reporting and calibration of post-bomb 14 C data. *Radiocarbon*, *46*(3), 1299–1304. https://doi.org/10.1017/S0033822200033154

Rietveld, H. M. (1969). A profile refinement method for nuclear and magnetic structures. *Journal of Applied Crystallography*, *2*(2), 65–71. https://doi.org/10.1107/S0021889869006558

Ruff, M., Szidat, S., Gäggeler, H. W., Suter, M., Synal, H. A., & Wacker, L. (2010). Gaseous radiocarbon measurements of small samples. *Nuclear Instruments and Methods in Physics Research Section B: Beam Interactions with Materials and Atoms*, *268*(7–8), 790–794. https://doi.org/10.1016/j.nimb.2009.10.032

Russell, M. J. (2018). Green rust: The simple organizing "seed" of all life? *Life*, *8*(3), 35. https://doi.org/10.3390/life8030035

Schaudinn, C., Stoodley, P., Kainović, A., O'Keeffe, T., Costerton, B., Robinson, D., et al. (2007). Bacterial biofilms, other structures seen as mainstream concepts. *Microbe Magazine*, *2*(5), 231–237. https://doi.org/10.1128/microbe.2.231.1

Schmid, T. W. (2011). Clumped—Isotopes—A new tool for for old questions: Case studies on biogenic and inorganic carbonates.

Schrenk, M. O., Kelley, D. S., Bolton, S. A., & Baross, J. A. (2004). Low archaeal diversity linked to subseafloor geochemical processes at the Lost City hydrothermal field, Mid-Atlantic Ridge. *Environmental Microbiology*, *6*(10), 1086–1095. https://doi.org/10.1111/j.1462-2920.2004.00650.x

Seyfried, W. E., Pester, N. J., Tutolo, B. M., & Ding, K. (2015). The Lost City hydrothermal system: Constraints imposed by vent fluid chemistry and reaction path models on subseafloor heat and mass transfer processes. *Geochimica et Cosmochimica Acta*, *163*, 59–79. https://doi.org/10.1016/j.gca.2015.04.040

Sokolov, I., Smith, D. S., Henderson, G. S., Gorby, Y. A., & Ferris, F. G. (2001). Cell surface electrochemical heterogeneity of the Fe(III)-reducing bacteria Shewanella putrefaciens. *Environmental Science and Technology*, *35*(2), 341–347. https://doi.org/10.1021/es001258s

Synal, H. A., Stocker, M., & Suter, M. (2007). MICADAS: A new compact radiocarbon AMS system. *Nuclear Instruments and Methods in Physics Research Section B: Beam Interactions with Materials and Atoms*, *259*(1), 7–13. https://doi.org/10.1016/j.nimb.2007.01.138

Tao, C., Seyfried, W. E., Lowell, R. P., Liu, Y., Liang, J., Guo, Z., et al. (2020). Deep high-temperature hydrothermal circulation in a detachment faulting system on the ultra-slow spreading ridge. *Nature Communications*, *11*(1), 1300. https://doi.org/10.1038/s41467-020-15062-w

Templeton, A. S., & Ellison, E. T. (2020). Formation and loss of metastable brucite: Does Fe(II)-bearing brucite support microbial activity in serpentinizing ecosystems? *Philosophical Transactions. Series A, Mathematical, Physical, and Engineering Sciences*, *378*(2165), 20180423. https://doi.org/10.1098/rsta.2018.0423

Ternieten, L., Früh-Green, G. L., & Bernasconi, S. M. (2021a). Carbonate mineralogy in mantle peridotites of the Atlantis massif (IODP expedition 357). *Journal of Geophysical Research: Solid Earth*, *126*(12), e2021JB021885. https://doi.org/10.1029/2021jb021885

Ternieten, L., Früh-Green, G. L., & Bernasconi, S. M. (2021b). Distribution and sources of carbon in serpentinized mantle peridotites at the Atlantis Massif (IODP expedition 357). *Journal of Geophysical Research: Solid Earth*, *126*(10), e2021JB021973. https://doi.org/10.1029/2021JB021973

Vogel, M. (2016). Peridotite-hosted hydrothermal systems past and present: Serpentinization, metasomatism and carbonate precipitation in modern and Jurassic ultramafic seafloor. https://doi.org/10.3929/ethz-a-010679089

Wacker, L., Bonani, G., Friedrich, M., Hajdas, I., Kromer, B., Němec, M., et al. (2010). Micadas: Routine and high-precision radiocarbon dating. *Radiocarbon*, *52*(2), 252–262. https://doi.org/10.1017/S0033822200045288

Wang, L., Putnis, C. V., King, H. E., Hövelmann, J., Ruiz-Agudo, E., & Putnis, A. (2017). Imaging organophosphate and pyrophosphate sequestration on brucite by in situ atomic force microscopy. *Environmental Science & Technology*, *51*(1), 328–336. https://doi.org/10.1021/acs.est.6b05456

Zwicker, J., Birgel, D., Bach, W., Richoz, S., Smrzka, D., Grasemann, B., et al. (2018). Evidence for archaeal methanogenesis within veins at the onshore serpentinite-hosted Chimaera seeps, Turkey. *Chemical Geology*, *483*(September 2017), 567–580. https://doi.org/10.1016/j.chemgeo.2018.03.027